

186
3-7-80

LA. 808

ornl

ORNL/TM-7161

MASTER

**OAK
RIDGE
NATIONAL
LABORATORY**

**UNION
CARBIDE**

**Nonlinear Coupling of
Tearing Modes with
Self-Consistent Resistivity
Evolution in Tokamaks**

B. Carreras
H. R. Hicks
J. A. Holmes
B. V. Waddell

OPERATED BY
UNION CARBIDE CORPORATION
FOR THE UNITED STATES
DEPARTMENT OF ENERGY

DISTRIBUTION OF THIS DOCUMENT IS UNLIMITED

DISCLAIMER

This report was prepared as an account of work sponsored by an agency of the United States Government. Neither the United States Government nor any agency Thereof, nor any of their employees, makes any warranty, express or implied, or assumes any legal liability or responsibility for the accuracy, completeness, or usefulness of any information, apparatus, product, or process disclosed, or represents that its use would not infringe privately owned rights. Reference herein to any specific commercial product, process, or service by trade name, trademark, manufacturer, or otherwise does not necessarily constitute or imply its endorsement, recommendation, or favoring by the United States Government or any agency thereof. The views and opinions of authors expressed herein do not necessarily state or reflect those of the United States Government or any agency thereof.

DISCLAIMER

Portions of this document may be illegible in electronic image products. Images are produced from the best available original document.

Printed in the United States of America. Available from
National Technical Information Service
U.S. Department of Commerce
5285 Port Royal Road, Springfield, Virginia 22161
NTIS price codes—Printed Copy: A05; Microfiche A01

This report was prepared as an account of work sponsored by an agency of the United States Government. Neither the United States Government nor any agency thereof, nor any of their employees, makes any warranty, express or implied, or assumes any legal liability or responsibility for the accuracy, completeness, or usefulness of any information, apparatus, product, or process disclosed, or represents that its use would not infringe privately owned rights. Reference herein to any specific commercial product, process, or service by trade name, trademark, manufacturer, or otherwise, does not necessarily constitute or imply its endorsement, recommendation, or favoring by the United States Government or any agency thereof. The views and opinions of authors expressed herein do not necessarily state or reflect those of the United States Government or any agency thereof.

ORNL/TM-7161

Dist. Category UC-20 g

Contract No. W-7405-eng-26

FUSION ENERGY DIVISION

NONLINEAR COUPLING OF TEARING MODES WITH SELF-CONSISTENT
RESISTIVITY EVOLUTION IN TOKAMAKS

B. Carreras,^{*} H. R. Hicks, J. A. Holmes, and B. V. Waddell[†]

Date Published - February 1980


DISCLAIMER

This book was prepared as an account of work sponsored by an agency of the United States Government. Neither the United States Government nor any agency thereof, nor any of their employees, makes any warranty, express or implied, or assumes any legal liability or responsibility for the accuracy, completeness, or usefulness of any information, apparatus, product, or process disclosed, or represents that its use would not infringe privately owned rights. Reference herein to any specific commercial product, process, or service by trade name, trademark, manufacturer, or otherwise, does not necessarily constitute or imply its endorsement, recommendation, or favoring by the United States Government or any agency thereof. The views and opinions of authors expressed herein do not necessarily state or reflect those of the United States Government or any agency thereof.

^a *Institute for Advanced Study, Princeton, New Jersey.

[†]Deceased September 14, 1978.

Prepared by the
OAK RIDGE NATIONAL LABORATORY
Oak Ridge, Tennessee 37830
operated by
UNION CARBIDE CORPORATION
for the
DEPARTMENT OF ENERGY

DISTRIBUTION OF THIS DOCUMENT IS UNLIMITED 

**THIS PAGE
WAS INTENTIONALLY
LEFT BLANK**

CONTENTS

ABSTRACT	1
I. INTRODUCTION	2
II. REDUCED SET OF RESISTIVE MAGNETOHYDRODYNAMIC EQUATIONS	6
III. EQUILIBRIUM CHARACTERISTICS	12
IV. NONLINEAR INTERACTION OF TEARING MODES: DESTABILIZATION DESTABILIZATION OF THE ($M = 3; N = 2$) TEARING MODE BY THE ($M = 2; N = 1$) MODE	25
V. NONLINEAR INTERACTION OF TEARING MODES: PROFILE DEPENDENCE	43
VI. COMPARISON WITH EXPERIMENT	54
VII. CONCLUSIONS	57
ACKNOWLEDGMENTS	59
REFERENCES	61

ABSTRACT

The nonlinear interaction of tearing modes of different helicity is studied for realistic values of the tokamak parameters of resistivity and parallel heat conduction. The self-consistent evolution of the resistivity is taken into account through the electron heat conduction equation. For equilibrium q profiles inferred from electron temperature profiles measured before a tokamak disruption, the essential result is that the $(m = 2; n = 1)$ mode nonlinearly destabilizes other modes on a rapid time scale. Because of the development of magnetic islands of different helicity, the toroidal current density is severely deformed. These islands overlap and field lines become stochastic in a sizable plasma volume, flattening the temperature profile in this region through parallel heat transport. The deformation of the toroidal current produces a rapid decrease in the self-inductance of the plasma, and the voltage at the limiter decreases, becoming increasingly negative. An extensive survey of equilibria and initial conditions has been conducted, and a simple prescription for their nonlinear stability properties is given.

I. INTRODUCTION

Previous papers^{1,2} have suggested that the nonlinear interaction of tearing modes of different helicity could be responsible for some of the disruptions observed in present-day tokamaks. This suggestion was based on the results of numerical studies of the nonlinear evolution of tearing modes in cylindrical geometry. These calculations had some limitations, as was duly acknowledged in Ref. 2. The resistivity was high compared with that of real tokamaks, the resistivity profile in the nonlinear evolution was held independent of time, and only two particular equilibrium q profiles were considered. The present paper removes these limitations. Presented here are results for realistic values of the resistivity and a study of the effect of its self-consistent evolution. Also, the exploration of a wide class of equilibria has given more generality to the previous results.

Understanding the detailed mechanism of tokamak disruptions is essential in devising methods to control or avoid them. This is not only important in improving tokamak confinement but also in suppressing the damaging effects of such disruptions on the device.

To study the nonlinear evolution of tearing modes, a reduced set of resistive magnetohydrodynamic equations was used,² and the self-consistent resistivity evolution was incorporated through the electron heat conduction equation. The results have been extended to more realistic tokamak parameters by the development of a new and more efficient three-dimensional code RSF,³ which uses a Fourier series expansion in the toroidal and poloidal angles and finite differences in the radial variable.

For a certain class of safety factor q profiles, which will be specified in Sec. V and which includes profiles observed before major tokamak disruptions,^{4,5} the $(m = 2; n = 1)$ and $(m = 3; n = 2)$ tearing modes are linearly unstable (here m and n denote the poloidal and toroidal mode number, respectively). Following the nonlinear evolution of this system reveals that the $(m = 3; n = 2)$ mode and other modes are nonlinearly destabilized on a rapid time scale by the $(m = 2; n = 1)$ mode. The order of the time scale is given by the $(m = 2; n = 1)$ linear growth rate. Because of this destabilization, islands of different helicity develop in the plasma. This severely deforms the current density profile in such a way that the plasma self-inductance decreases and the voltage at the limiter drops, becoming increasingly negative at the end of the calculations, in agreement with the "negative voltage spikes" observed experimentally. The overlap of islands leads to the stochastization of the magnetic field lines in a sizable plasma volume, flattening the temperature profile in this region through parallel heat transport. When the magnetic field lines have become stochastic in a finite volume, modes having singular surfaces in this region are further destabilized with growth rates several times bigger than the linear growth rates.

The low value of the resistivity separates the time scales involved in the problem. This allows clear observation of the different dynamical regimes present in the time evolution of the tearing modes. When the calculation is initialized with very small perturbations, three different regimes successively appear. First, the initialized modes that are unstable grow exponentially with time in what is practically a linear regime. Second, when the magnetic islands

have grown beyond the tearing layer width, nonlinear effects become important, with the result that the islands grow linearly with time as if only modes of a single helicity were present.⁶ Finally, after the magnetic islands touch, there is strong destabilization of the modes involved and the growth is again approximately exponential, as just described. In cases where the unstable modes saturate before their corresponding islands touch, this final exponential phase is absent.

In the highly nonlinear phase of the calculation, after the strong destabilization of the $(m = 3; n = 2)$ mode, more and more modes with high m and/or n values are nonlinearly generated. This implies that increasingly small scale lengths become involved in this process and that a fluid model can no longer describe it. This dictates the end of the calculation.

A wide spectrum of equilibrium q profiles was studied to provide a better understanding of the characteristics of the nonlinear interaction. However, since this analysis is for cylindrical geometry, these profiles are restricted to $q(0) > 1$ because the toroidal coupling between the $(m = 1; n = 1)$ and $(m = 2; n = 1)$ could be important in cases where the safety factor is below unity.⁷ A very general result is that the strong destabilization of the $(m = 3; n = 2)$ mode occurs for q profiles such that

$$r_{21} - r_{32} < \frac{1}{2}(W_{21} + W_{32}),$$

where r_{mn} is the radial position of the singular surface for the $(m; n)$ mode and W_{mn} is its single-helicity saturated island width. For all the cases considered here, the rapid destabilization of the

($m = 3; n = 2$) mode by the ($m = 2; n = 1$) mode starts after the two magnetic islands touch. Apparently the usual resistive flow effects, which reduce the mode growth from exponential to linear,⁶ are not operative in this explosive growth phase because the magnetic flux surfaces are being destroyed.

The present results confirm those obtained when resistivity evolution is not taken into account,¹ except that here the disruption proceeds somewhat faster. These low resistivity calculations allow a more distinct separation of time scales in the different phases of the nonlinear evolution.

The body of this paper is organized as follows: In Sec. II, the reduced set of resistive magnetohydrodynamic equations used in our calculations is presented. In Sec. III, the equilibrium q profiles and their stability properties from the standpoint of linear and nonlinear theory are discussed. A description of the nonlinear interaction of tearing modes for an equilibrium state like the one before a major disruption in the Princeton Large Torus (PLT) tokamak is presented in Sec. IV. In Sec. V, the results of a q profile exploration are given and compared with an analytical model. Finally, in Sec. VI, the characteristic time scale for the nonlinear process is discussed and the results are compared with experiment.

II. REDUCED SET OF RESISTIVE MAGNETOHYDRODYNAMIC EQUATIONS

The resistive magnetohydrodynamic equations are

$$\rho_m \left(\frac{\partial \vec{v}}{\partial t} + \vec{v} \cdot \nabla \vec{v} \right) = - \nabla p + \vec{J} \times \vec{B}, \quad (1)$$

$$\frac{\partial \vec{B}}{\partial t} = - \nabla \times \vec{E}, \quad (2)$$

$$\vec{J} = \frac{1}{\mu_0} \nabla \times \vec{B}, \quad (3)$$

and

$$\vec{E} = \eta \vec{J} - \vec{v} \times \vec{B}, \quad (4)$$

where \vec{v} is the fluid velocity, ρ_m is the mass density, p is the pressure, \vec{B} is the magnetic field, \vec{J} is the current density, \vec{E} is the electric field, η is the resistivity, and μ_0 is the vacuum magnetic permeability. To close this system of equations, it is necessary to specify an equation of state and equations for the resistivity and mass density. The equation for the resistivity will be discussed later. In this paper, the mass density is assumed to be constant in space and time. This is consistent with the continuity equation for the mass density. The equation of state will be a consequence of the simplifying assumptions that will be used to reduce the system of magnetohydrodynamic equations.

Standard tokamak ordering allows the reduction of the resistive magnetohydrodynamic equations to a set of two partial differential equations in two unknowns. It is assumed that $\epsilon \equiv a/R_0 \ll 1$, where a and R_0 are the minor and major radii of the torus, respectively. The toroidal field perturbation is given by

$$\tilde{B}_\zeta \cong \epsilon^2 B_{\zeta 0}, \quad (5)$$

where \sim and o denote perturbed and unperturbed quantities and ζ is the toroidal angle. Contributions only to the lowest order in ϵ are considered, thereby eliminating the fast magnetohydrodynamic time scale associated with the Alfvén waves propagating in the poloidal direction. A second assumption is introduced when the calculations are restricted to low β plasmas (i.e., $\beta \approx \epsilon^2$). These two hypotheses in cylindrical geometry allow the toroidal component of the fluid velocity to be neglected and imply that the fluid is incompressible.

A detailed derivation of the reduced set of resistive magnetohydrodynamic equations based on the previously stated hypotheses is given in Ref. 2. These equations in dimensionless form are

$$\frac{\partial \Psi}{\partial t} = \eta J_\zeta - E_\zeta^w - \frac{\partial \Psi}{\partial r} \frac{1}{r} \frac{\partial \Phi}{\partial \theta} + \frac{1}{r} \frac{\partial \Psi}{\partial \theta} \frac{\partial \Phi}{\partial r} - \frac{\partial \Phi}{\partial \zeta}, \quad (6)$$

$$\frac{\partial U}{\partial t} + \frac{1}{r} \frac{\partial \Phi}{\partial \theta} \frac{\partial U}{\partial r} - \frac{\partial \Phi}{\partial r} \frac{1}{r} \frac{\partial U}{\partial \theta} = S^2 \left(\frac{1}{r} \frac{\partial \Psi}{\partial \theta} \frac{\partial J_\zeta}{\partial r} - \frac{\partial \Psi}{\partial r} \frac{1}{r} \frac{\partial J_\zeta}{\partial \theta} - \frac{\partial J_\zeta}{\partial \zeta} \right), \quad (7)$$

$$U = \nabla_\perp^2 \Phi, \quad (8)$$

and

$$J_{\zeta} = \nabla_{\perp}^2 \Psi . \quad (9)$$

Here r , θ , and ζ are the usual toroidal coordinates (radial, poloidal, and toroidal, respectively). Because all toroidal effects are neglected, $\zeta = \frac{z}{R_0}$, where z is the coordinate along the cylinder. All lengths have been normalized to the minor radius a ; the resistivity to some typical value $\bar{\eta}$ [in general, $\bar{\eta}$ is such that $\eta(0) = 1$]; and the time to the resistive diffusion time $\tau_r = (a^2 \mu_0) / \bar{\eta}$. The functions Ψ and Φ are the poloidal flux and velocity stream functions, normalized to $a^2 B_{\zeta 0}$ and $a^2 B_{\zeta 0} / \tau_r$, respectively. They are related to the magnetic field and fluid velocity by

$$\vec{B} = B_{\zeta 0} (-\epsilon \nabla_{\perp} \Psi \times \hat{\zeta} + \hat{\zeta}) \quad (10)$$

and

$$\vec{v}_{\perp} = \frac{a}{\tau_r} (\nabla_{\perp} \Psi \times \hat{\zeta}) , \quad (11)$$

where $\hat{\zeta}$ is a unit vector in the toroidal direction and the subscript \perp indicates perpendicularity to $\hat{\zeta}$. The toroidal current density is

$$J_t = \frac{B_{\zeta 0}}{\mu_0 R_0} J_{\zeta} , \quad (12)$$

and U is the toroidal component of the vorticity. The parameter S is the ratio of the two time scales involved in this problem: $S =$

τ_r/τ_{hp} , where τ_{hp} is the poloidal Alfvén time, or the time for Alfvén waves to propagate in the toroidal direction, $\tau_{hp} = R_o(\mu_o \rho_m)^{1/2}/B_{\zeta o}$.

This reduced set of three-dimensional equations was first derived by H. R. Strauss⁸ for rectangular geometry with the resistivity term omitted. He used them to study the nonlinear evolution of ideal magnetohydrodynamic modes. Assuming helical symmetry, these equations reduce to the ones derived in Ref. 9. These equations, in three-dimensional cylindrical form, have been used in Refs. 1, 2, and 10 to study the nonlinear interaction of tearing modes in cylindrical geometry.

Two different models have been used for the resistivity. The simplest assumption is to take η independent of time throughout the whole evolution. In this case, its radial dependence is obtained by assuming a constant loop voltage in the equilibrium and not allowing the magnetic flux to evolve in the absence of tearing mode activity, which implies

$$\eta(r) = \eta(a) \frac{J_{\zeta}(a)}{J_{\zeta}(r)}. \quad (13)$$

A second possibility is to introduce a self-consistent resistivity evolution through the electron heat conduction equation

$$\frac{3}{2}n_e \left(\frac{\partial T_e}{\partial t} + \vec{v} \cdot \vec{\nabla}_{\perp} T_e \right) = K_{\parallel} \nabla_{\parallel}^2 T_e + K_{\perp} \nabla_{\perp}^2 T_e + \eta J_{\zeta}^2 \quad (14)$$

and to use the Spitzer relation between resistivity and electron temperature

$$\eta \propto T_e^{-3/2} . \quad (15)$$

In Eq. (14),

$$\vec{\nabla}_{\parallel} \equiv \frac{\vec{B}}{|\vec{B}|} \cdot \vec{\nabla} , \quad (16)$$

n_e is the electron number density, and K_{\parallel} and K_{\perp} are the parallel and perpendicular heat conduction coefficients, which are assumed to be constant. In dimensionless form, Eq. (14) becomes

$$\frac{\partial T}{\partial t} + \frac{1}{r} \frac{\partial \Phi}{\partial \theta} \frac{\partial T}{\partial r} - \frac{\partial \Phi}{\partial r} \frac{1}{r} \frac{\partial T}{\partial \theta} = \bar{\chi}_{\parallel} \nabla_{\parallel}^2 T + \bar{\chi}_{\perp} \nabla_{\perp}^2 T + g \eta J_{\zeta}^2 , \quad (17)$$

where $\bar{\chi}_{\parallel} = (2\tau_r K_{\parallel}) / (3R_0^2 n_e)$, $\bar{\chi}_{\perp} = (2\tau_r K_{\perp}) / (3a^2 n_e)$, and $g = (2\bar{\tau}_r B_{\zeta 0}) / (3T n_c R_0)$. T has been normalized in such a way that $\eta = T^{3/2}$.

The reduced set of magnetohydrodynamic equations contains three dimensionless parameters: S , $\bar{\chi}_{\parallel}$, and $\bar{\chi}_{\perp}$. From the point of view of the numerical calculations, the parameters S and $\bar{\chi}_{\parallel}$ play a critical role. Realistic plasma parameters for a device like PLT are $S = 10^7$ and $\bar{\chi}_{\parallel} / \bar{\chi}_{\perp} = 10^9$. These values indicate the disparity of time scales that must be followed in the calculation. This is one of the most serious difficulties in solving the problem numerically. A three-dimensional code, RSF,³ has been developed to numerically time-advance Eqs. (6), (7), and (17). The quantities Ψ and Φ are expanded in Fourier series in the toroidal and poloidal angles to give

$$\Psi = \sum_{m,n} \psi_{mn}(r) \cos (m\theta + n \zeta) \quad (18)$$

and

$$\Phi = \sum_{m,n} \phi_{mn}(r) \sin (m\theta + n\zeta) , \quad (19)$$

and a finite difference scheme is employed in the radial variable. This has proved to be more efficient than a previous scheme² that was based on finite differences in the three coordinates. The use of both codes has allowed a careful checking of the numerics. More details on numerics are given elsewhere.³

The results presented here use about 30 Fourier components, although some cases include up to 60. The radial grid for high S calculations has between 200 and 300 points. In general, a nonuniform radial grid has been used to allow the grid points to be concentrated where they are needed. For high S values, the typical mesh size in the region where the grid is concentrated is $\Delta r = 2.5 \times 10^{-3}$.

III. EQUILIBRIUM CHARACTERISTICS

In the cylindrical geometry limit, the tokamak equilibrium is specified by a given safety factor profile $q(r)$. For Eqs. (6)-(9), an exact equilibrium solution can be written as

$$\phi_{\text{eq}} = 0 ,$$

$$\psi_{\text{eq}}(r) = \int_r^1 \frac{r' dr'}{q(r')} ,$$

$$n_{\text{eq}}(r) = \frac{E_{\xi}^w}{J_{\text{eq}}(r)} . \quad (20)$$

In the calculations presented here, the equilibrium has been defined using either an analytical parameterization of the q profile or a spline interpolation of a few radial values of q inferred from experimental values of the electron temperature. For discussing the stability properties of the equilibria, it is useful to parameterize the q profiles in a simple way:

$$q(r) = q(0) \left\{ 1 + r^{2\lambda} \left[\left(\frac{q_{\ell}}{q(0)} \right)^{\lambda} - 1 \right] \right\}^{1/\lambda} . \quad (21)$$

The safety factor profile is then specified by three parameters: its value at the limiter q_{ℓ} , its value at the magnetic axis $q(0)$, and λ . For $\lambda = 1, 2,$ and 4 , this parameterization corresponds to the peaked, round, and flat profiles introduced in Ref. 11. As an example, $q(0) = 1.08$ and $q_{\ell} = 4.2$ have been fixed, and the corresponding profiles for λ

$m = 1, 2,$ and 4 have been plotted in Fig. 1. It is clear from this figure that with increasing λ , the profiles became flatter near the magnetic axis.

As stated in the introduction, the main motivation for the study of the nonlinear interaction of tearing modes is to understand the mechanism of a major disruption in a tokamak. It has already been found that for a limited number of equilibria,^{1,2} the nonlinear interaction of the $(m = 2;n = 1)$ and $(m = 3;n = 2)$ tearing modes could explain some of the characteristics of a tokamak disruption. This paper will explore further the dynamics of this interaction by studying a wider class of equilibria and using realistic tokamak parameters. However, because the toroidal effects are absent in the equations employed, the range of q values will be restricted to a region where these effects are not expected to be important. Therefore, only q profiles with $q \geq 1$ will be considered, because for $q < 1$ the toroidal coupling between the $(m = 1;n = 1)$ and $(m = 2;n = 1)$ modes could certainly be as important as the nonlinear coupling. Also, the range of q values corresponds to "normal" tokamak operation, namely $3 < q_\ell < 5$ and $q(0) < 1.5$. For this range of parameters, no more than two linearly unstable modes in cylindrical geometry have been found, namely, the $(m = 2;n = 1)$ and $(m = 3;n = 2)$ modes. This paper will be mainly concerned with equilibria in which the $(m = 2;n = 1)$ mode has high potential energy and the nonlinear interaction of this mode with the $(m = 3;n = 2)$ mode is likely to be strong.

ORNL-DWG 79-2103R FED

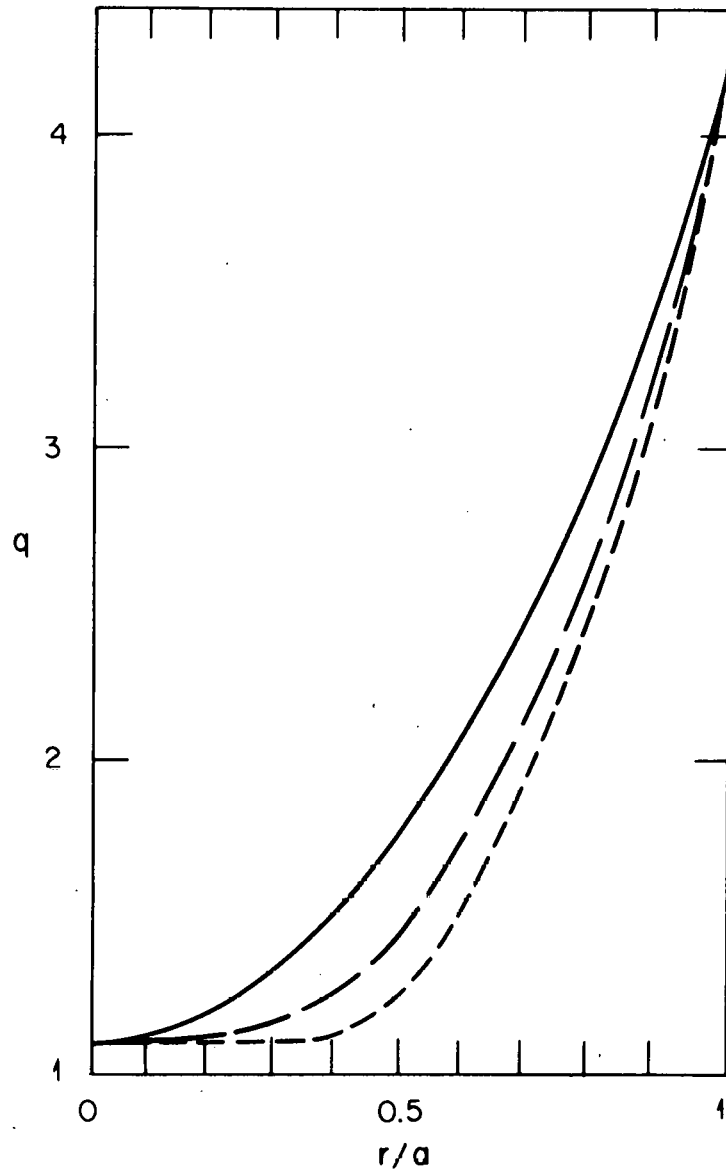


FIG. 1. Safety factor q profile given by Eq. (21) for $\lambda = 1$ (—), $\lambda = 2$ (---), and $\lambda = 4$ (-·-·-). At the origin $q(0) = 1.08$ and at the limiter $q_\ell = 4.2$.

In linear tearing mode theory, the potential energy δW of a mode is proportional to Δ' ,¹² where Δ' is the discontinuity in the radial derivative of the flux function at the corresponding singular surface. For an $(m;n)$ mode, Δ' is defined¹¹ as

$$\Delta'_{mn} = \lim_{\delta \rightarrow 0} \left(\frac{d\psi_{mn}}{dr} \Big|_{r_+} - \frac{d\psi_{mn}}{dr} \Big|_{r_-} \right) / \psi_{mn}(r_{mn}), \quad (22)$$

where r_{mn} is the radial position of the singular surface, $q(r_{mn}) = m/n$, and $r_{\pm} = r_{mn} \pm \delta$. For fixed values of $q(0)$ and q_0 , the value of Δ' for the $(m = 2;n = 1)$ mode does not change much with λ , as can be seen in Fig. 2. The same figure shows that the Δ' for the $(m = 3;n = 2)$ mode increases with λ , making this mode linearly unstable for $\lambda > 1.5$. For both modes, Δ' increases with $q(0)$ and their stability properties are very sensitive to $q(0)$ when $q(0)$ is ~ 1 (see Fig. 3).

The nonlinear evolution of an $(m;n)$ tearing mode with $m > 1$, in the single-helicity approximation, is no longer exponential with time when the island width of the mode exceeds its tearing layer width.⁶ The width of the magnetic island associated with the mode increases linearly with time, and the mode saturates at a finite island width.¹³ The saturated island width is a measure of the level of the instability in the nonlinear regime, and its magnitude can be correlated with an experimentally measurable quantity,¹⁴ the poloidal field fluctuation at the limiter. In addition to Δ' , the saturation island width for the $(m = 2;n = 1)$ and $(m = 3;n = 2)$ modes has been plotted as a function of λ in Fig. 2. The saturated island width for the $m = 2$ mode increases dramatically with λ , and the $m = 2$ magnetic island encompasses more than 20% of the plasma radius for $\lambda = 4$. This

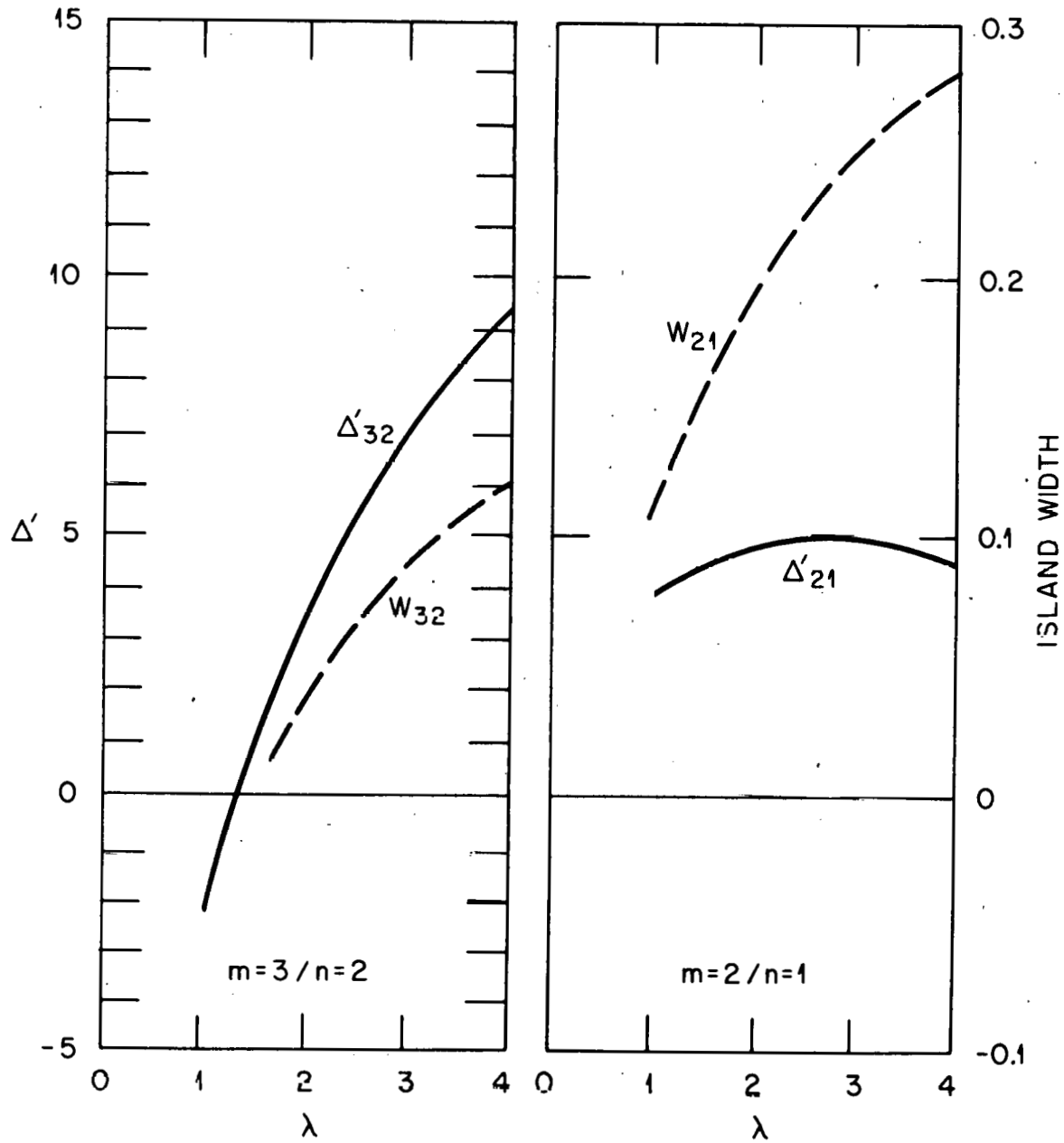


FIG. 2. Δ' and the saturation island width W for the $(m = 3; n = 2)$ and $(m = 2; n = 1)$ modes as a function of λ . The equilibrium q profiles are given by Eq. (21) with $q(0) = 1.08$ and $q_L = 4.2$.

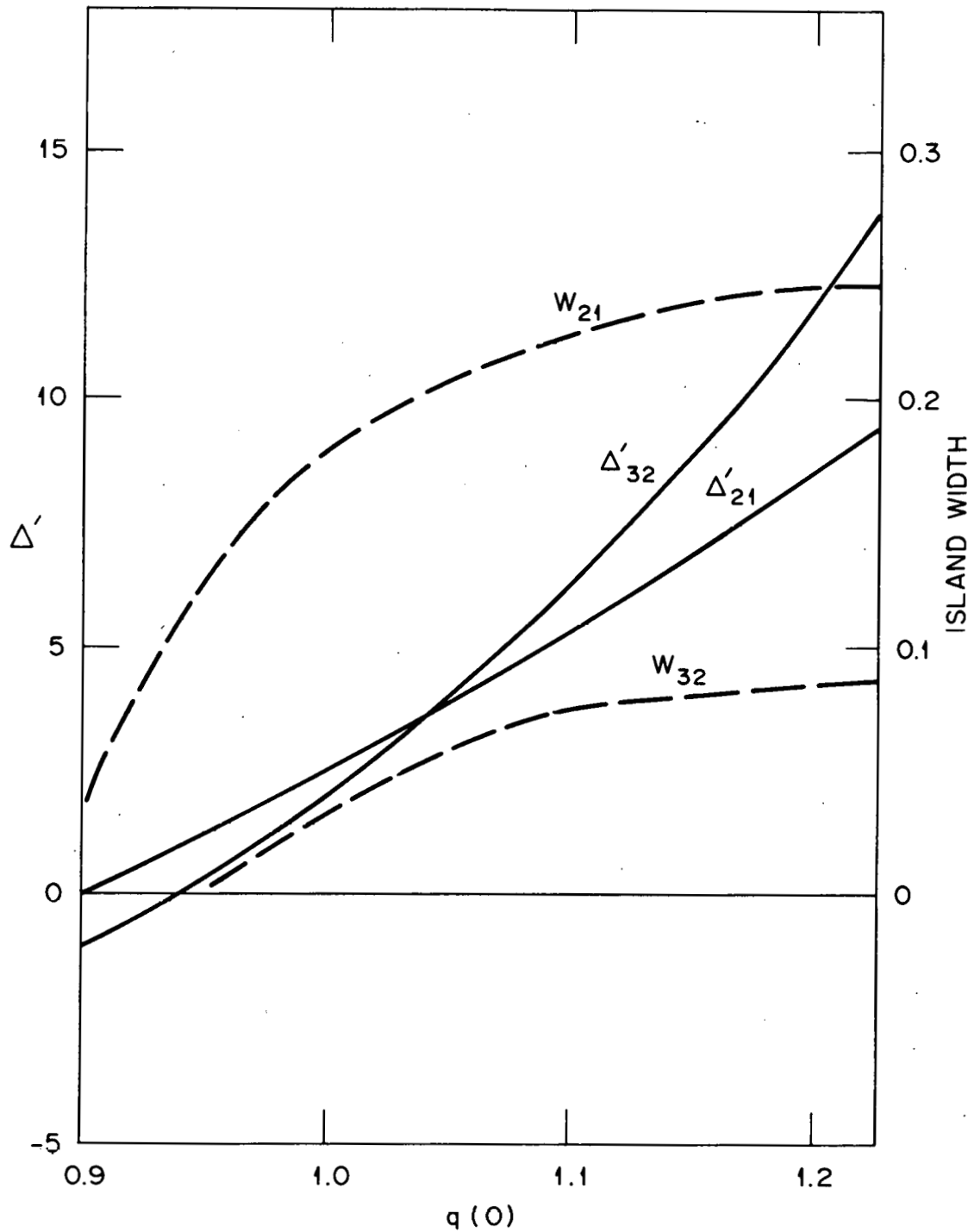


FIG. 3. Δ' and the saturation island width W for the $(m = 2; n = 1)$ and $(m = 3; n = 2)$ modes as a function of $q(0)$. The equilibrium q profiles are given by Eq. (21) with $\lambda = 3.5$ and $q_{\ell} = 4.2$.

fact has been stressed in Ref. 15. The equilibria characterized by q profiles with λ near 4 have a high level of tearing mode activity. Moreover, when λ increases, the q profile becomes steeper between the $q = 1.5$ and $q = 2$ surfaces (see Fig. 1). This means that the surfaces get closer to each other and the chance of a strong nonlinear interaction between the $(m = 2; n = 1)$ and $(m = 3; n = 2)$ modes becomes more likely. For these reasons, q profiles with $\lambda > 2$ and profiles with analogous properties will be studied in detail in this paper. Profiles of this type have been experimentally measured before some major disruptions in tokamaks.^{4,5} These will be considered specifically in forthcoming sections.

For the results shown in Figs. 2-3, the resistivity was kept constant in time. In this case, for the parameterization of q given in Eq. (21), the resistivity profile normalized to 1 at the magnetic axis is

$$\eta(r) = \left\{ 1 + r^{2\lambda} \left[\left(\frac{q_\ell}{q(0)} \right)^\lambda - 1 \right] \right\}^{1+1/\lambda}. \quad (23)$$

The resistivity at the singular surface for the $(m;n)$ mode increases exponentially with λ : $\eta(r_{mn}) = [m/nq(0)]^{\lambda+1}$. Therefore, the linear growth rate for the $(m = 2; n = 1)$ and $(m = 3; n = 2)$ modes increases with λ not only because Δ' increases, but also because the resistivity increases. The linear growth rates for both modes have been plotted in Fig. 4.

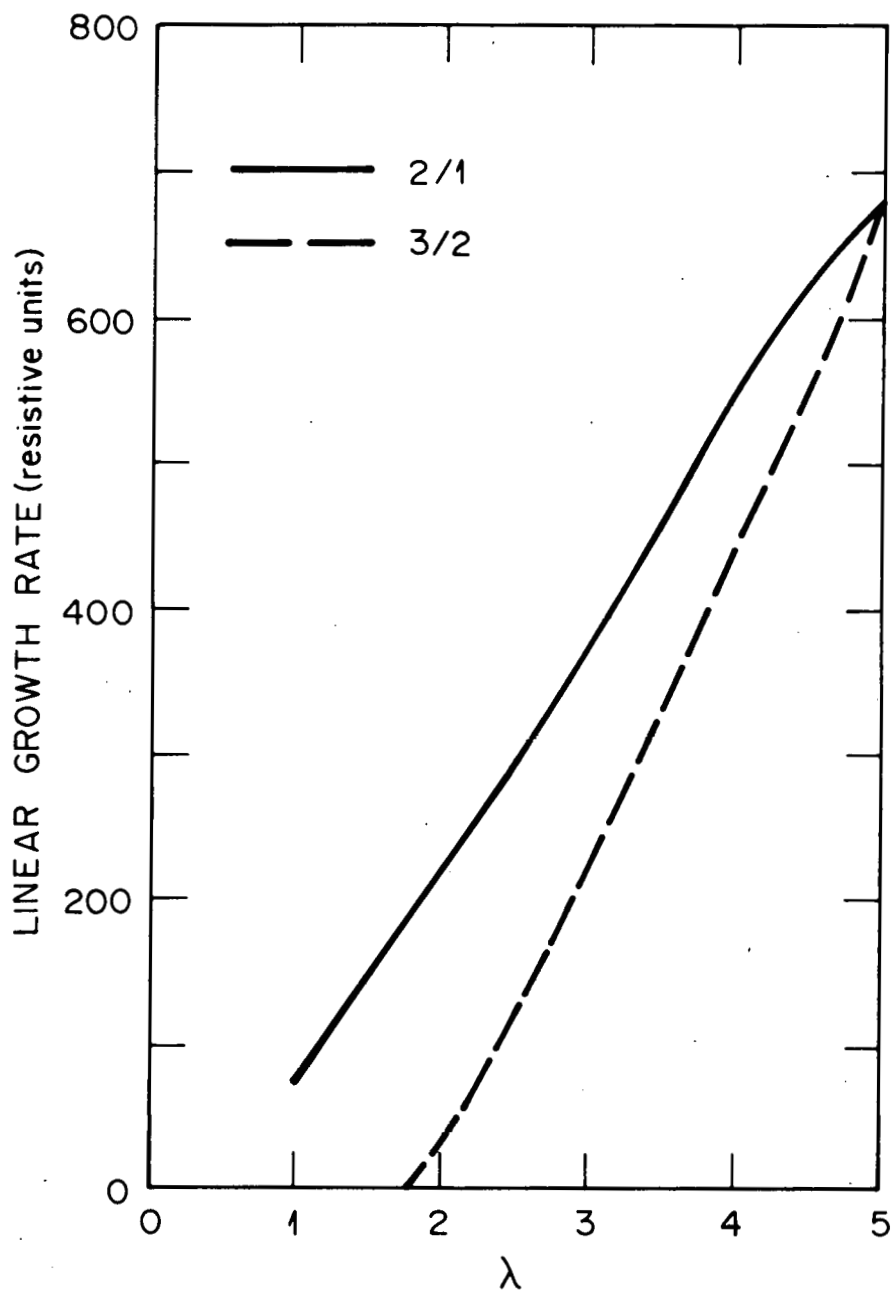


FIG. 4. Linear growth rates for the $(m = 2; n = 1)$ and $(m = 3; n = 2)$ modes as a function of λ for the same q profile as Fig. 2. The value of S at the magnetic axis is 2×10^4 for all cases considered.

When the self-consistent evolution of the resistivity is taken into account, there is no qualitative change in previous results for realistic tokamak parameters. In this case, the parallel transport term should dominate in Eq. (17), which requires $\bar{\chi}_{\parallel}$ to be greater than 10^6 . The linear growth rates are above the values obtained when the resistivity is kept constant in time. In Fig. 5, the ($m = 2; n = 1$) growth rate is plotted as a function of $\bar{\chi}_{\parallel}$ for a typical equilibrium at $S = 10^6$. The broken line in Fig. 5 is the value of the growth rate when the resistivity does not evolve in time.

The nonlinear regime is not substantially modified by the resistivity evolution if $\bar{\chi}_{\parallel} > 10^6$. In Fig. 6, the ($m = 2; n = 1$) island width evolution is shown for different values of $\bar{\chi}_{\parallel}$ and compared with the case in which the resistivity is constant in time (broken line). For increasing $\bar{\chi}_{\parallel}$, the continuous lines tend toward the broken line. There apparently is a change of regime when $\bar{\chi}_{\parallel}$ is too small. In such cases, the convective term dominates the electron heat conduction equation [Eq. (17)], the 2/1 magnetic island grows fast, and does not saturate. Also, modes with large m that otherwise are stable become linearly unstable. This change of regime is also apparent when the temperature contours are compared with the ($m = 2; n = 1$) helical flux contours. In the single-helicity approximation, the helical flux function ψ_p^* can be written in terms of the poloidal flux function Ψ as

$$\psi_p^* = -p \left[\psi_{00} + \sum_{m/n=p} \psi_{mn} \cos(m\theta + n\zeta) \right] - \frac{1}{2}(r^2 - 1), \quad (24)$$

where $p = m/n$ and ψ_p^* has been normalized to $a^2 B_0$. Plotted in Fig. 7 are the ψ_2^* contours and the temperature contours for two different $\bar{\chi}_{\parallel}$

ORNL-DWG 79-2052 FED

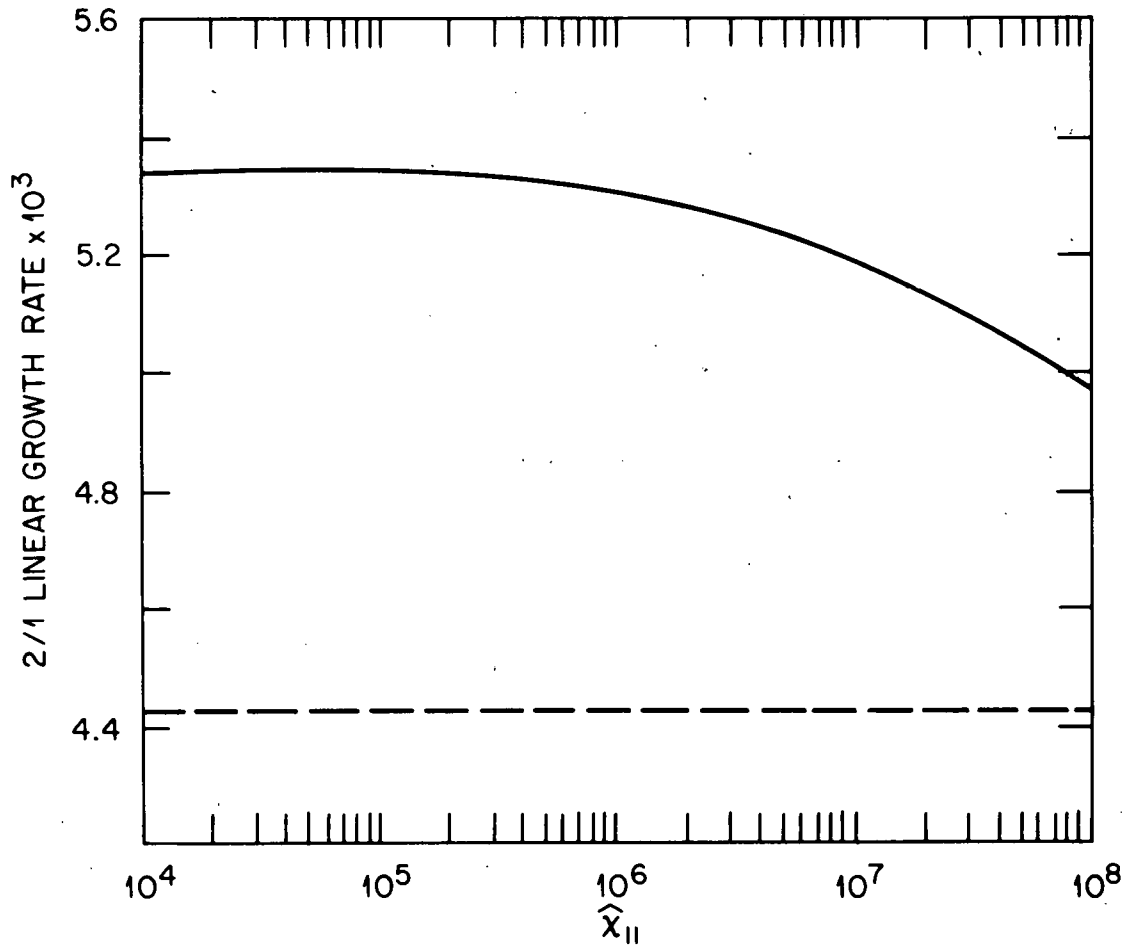


FIG. 5. Linear growth rate for the ($m = 2; n = 1$) mode as a function of $\widehat{\chi}_{\parallel}$ (continuous line) compared with its value when the resistivity is kept constant in time (broken line). The q profile is the one considered in Sec. IV, and $S = 10^6$ at $r = 0$.

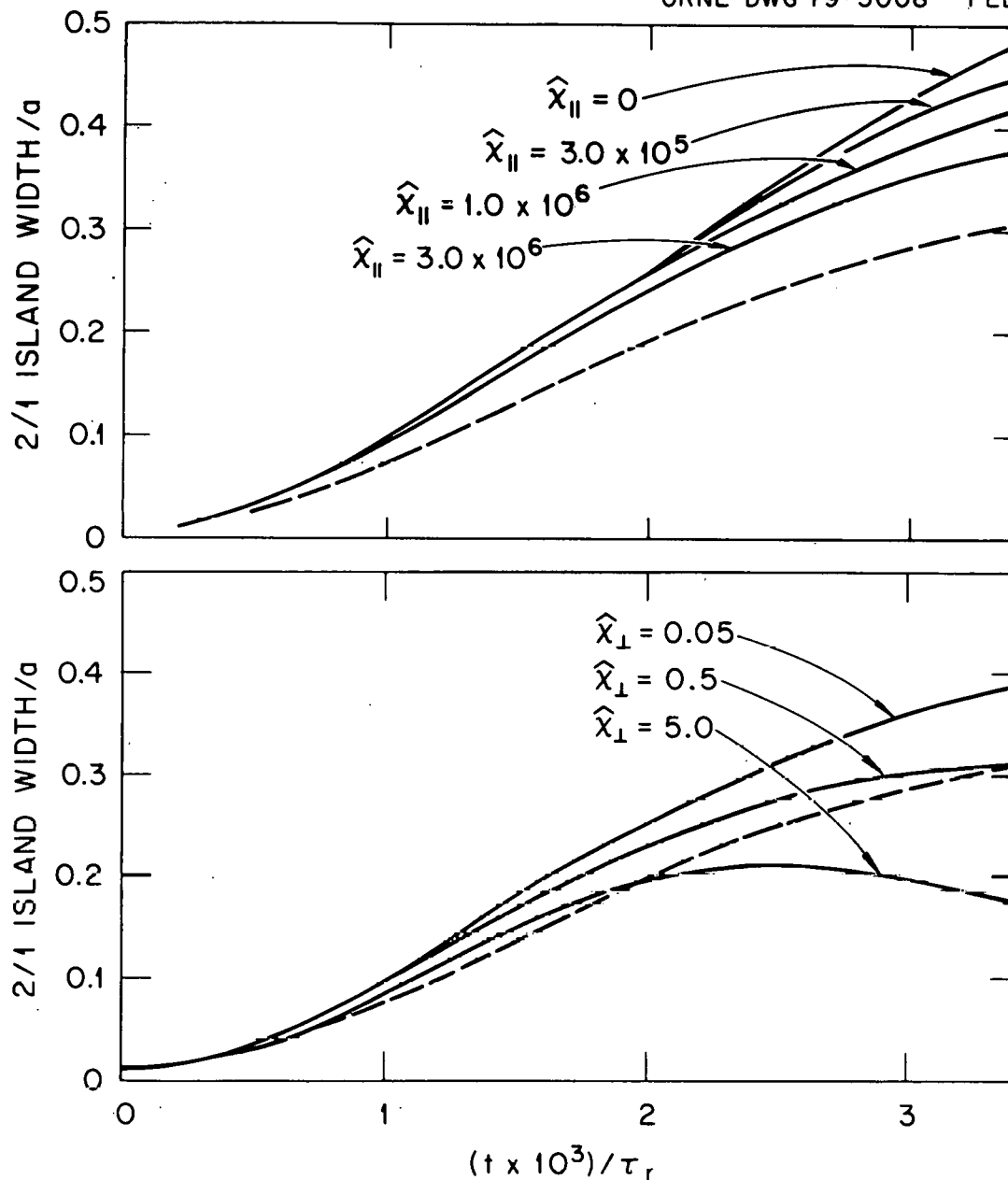


FIG. 6. The 2/1 island width as a function of time for different values of $\bar{\chi}_{\parallel}$ with $\bar{\chi}_{\perp} = 0.1$ (top) and for different values of $\bar{\chi}_{\perp}$ with $\bar{\chi}_{\parallel} = 3 \times 10^6$ (bottom). The broken line corresponds to the case with no resistivity evolution. The equilibrium q profile and S value are the same as in Fig. 5.

ORNL-DWG 79-2429R FED

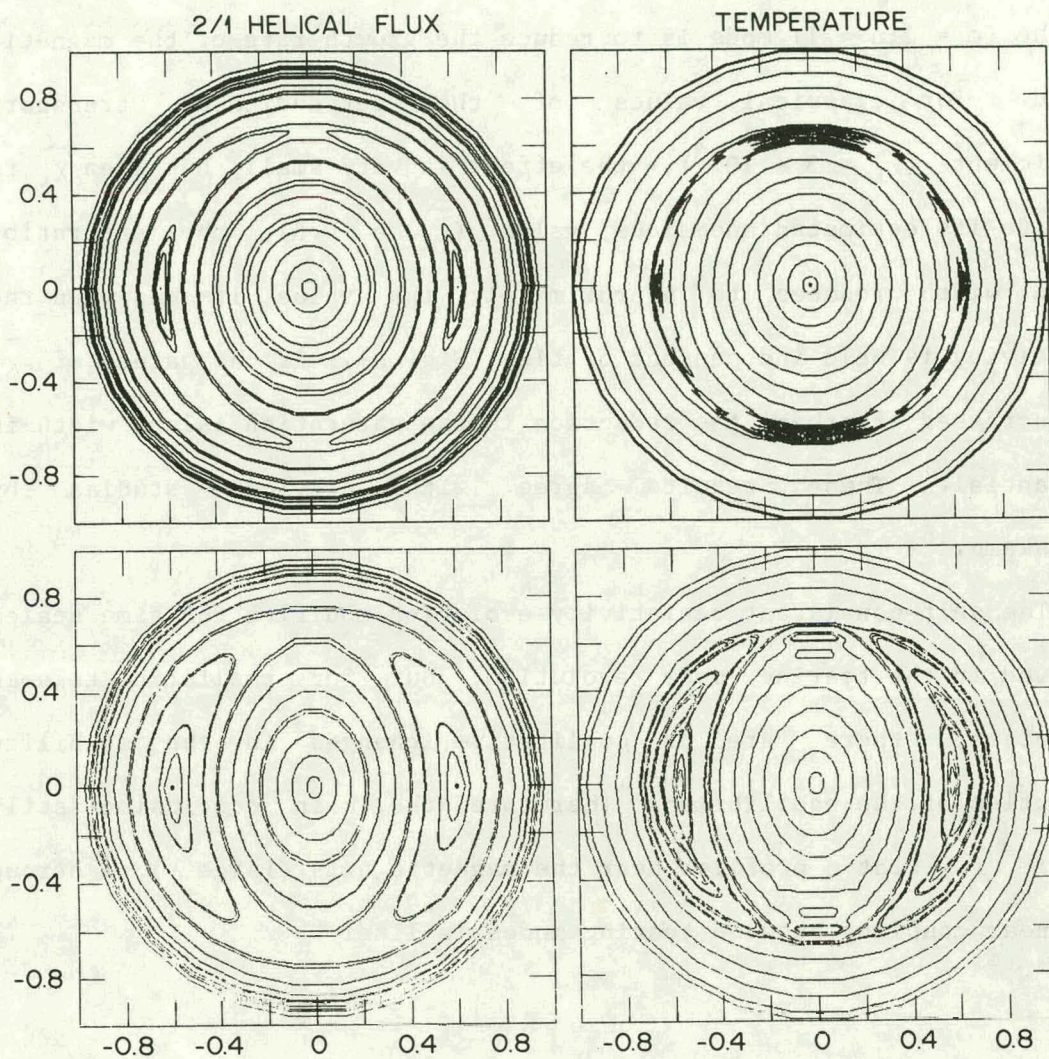


FIG. 7. Comparison between the 2/1 helical flux contours and temperature contours for $\bar{\chi}_{\parallel} = 0$ (top) and $\bar{\chi}_{\parallel} = 10^7$ (bottom) in a single-helicity calculation. In the second case, the temperature has become a function of the helical flux function.

values. It should be noted that for the larger value of $\bar{\chi}_{\parallel}$, the temperature becomes a function of ψ_2^* only.

The effect of perpendicular transport on the nonlinear evolution of the ($m = 2; n = 1$) mode is to reduce the growth rate of the magnetic island. For classical values of the perpendicular transport coefficient ($\bar{\chi}_{\perp} = 3 \times 10^{-3}$), the effect is very small, but when $\bar{\chi}_{\perp}$ is close to its estimated anomalous value ($\bar{\chi}_{\perp} = 0.5$), the saturation island width reduces to approximately the value it has when the resistivity is held independent of time (Fig. 6). If the value of $\bar{\chi}_{\perp}$ is increased further, the reduction in the saturation island width is substantial. These results agree with previous studies by D. Biskamp.¹⁶

The self-consistent resistivity evolution modifies the time scales involved in the tearing mode evolution, but for realistic tokamak parameters, there are no qualitative changes in the stability properties of the equilibrium. Therefore, the main conclusion still holds: for flat q profiles near the magnetic axis (large λ), a strong nonlinear coupling between tearing modes is likely.

IV. NONLINEAR INTERACTION OF TEARING MODES: DESTABILIZATION OF THE
($m = 3; n = 2$) TEARING MODE BY THE ($m = 2; n = 1$) MODE

This section describes a typical case in which the ($m = 2; n = 1$) and ($m = 3; n = 2$) nonlinear interaction leads to explosive growth and to stochastization of field lines. As an example, consider an equilibrium characterized by a q profile obtained from fitting the electron temperature profile measured in the PLT tokamak before a major disruption.⁴ This profile is well described by Eq. (21) taking $q(0) = 1.34$, $q_0 = 4.2$, and $\lambda = 3.24$, which is very similar to the profile studied in Refs. 1 and 2.

The nonlinear evolution of the system will be considered with the assumption that the ($m = 2; n = 1$) and ($m = 3; n = 2$) modes have been initially perturbed. The results are summarized in Fig. 8, where, to simplify the drawing, the time evolution of only three magnetic islands is plotted. For each helicity, the magnetic island width is calculated as if only this helicity were present in the plasma. Each island width is plotted in its proper radial location (see Fig. 8). For $t < 1.4 \times 10^{-3} \tau_r$, the evolution of the ($m = 2; n = 1$) and ($m = 3; n = 2$) modes proceeds as if the other modes were not present. Their island widths grow linearly with time, as in the single-helicity approximation.⁶ But when two magnetic islands begin to overlap, the modes start growing on a faster time scale. In particular, when the 2/1 and 3/2 magnetic islands overlap at $t = 1.7 \times 10^{-3} \tau_r$, the ($m = 3; n = 2$) mode is strongly destabilized. Its nonlinear growth rate increases (see Fig. 9) and, in a very short time, $\Delta t = 0.20 \times 10^{-3} \tau_r$ [of the order of the inverse of the ($m = 2; n = 1$) linear growth rate], its magnetic island width becomes $>0.1a$. During this interval, many modes are

ORNL-DWG 79-2513 FED

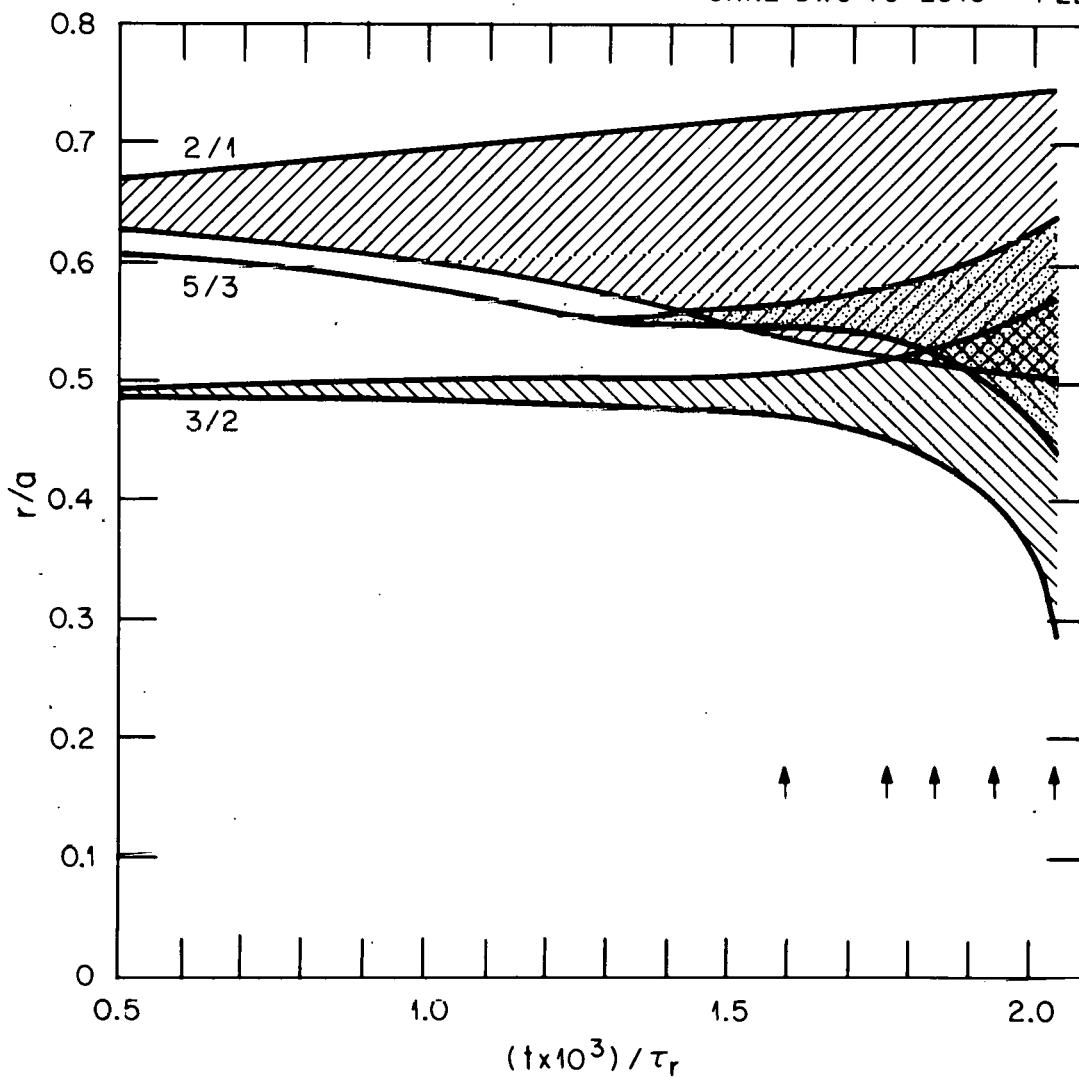


FIG. 8. Time evolution of the magnetic island width for the $(m = 2; n = 1)$, $(m = 3; n = 2)$, and $(m = 5; n = 3)$ modes in a multiple-helicity calculation. The q profile is the one considered in Sec. IV with $S = 10^6$, $\bar{\chi}_{\parallel} = 10^7$, and $\bar{\chi}_{\perp} = 0.05$.

NONLINEAR DESTABILIZATION OF THE 3/2 MODE

ORNL DWG 79-2113R2 FED

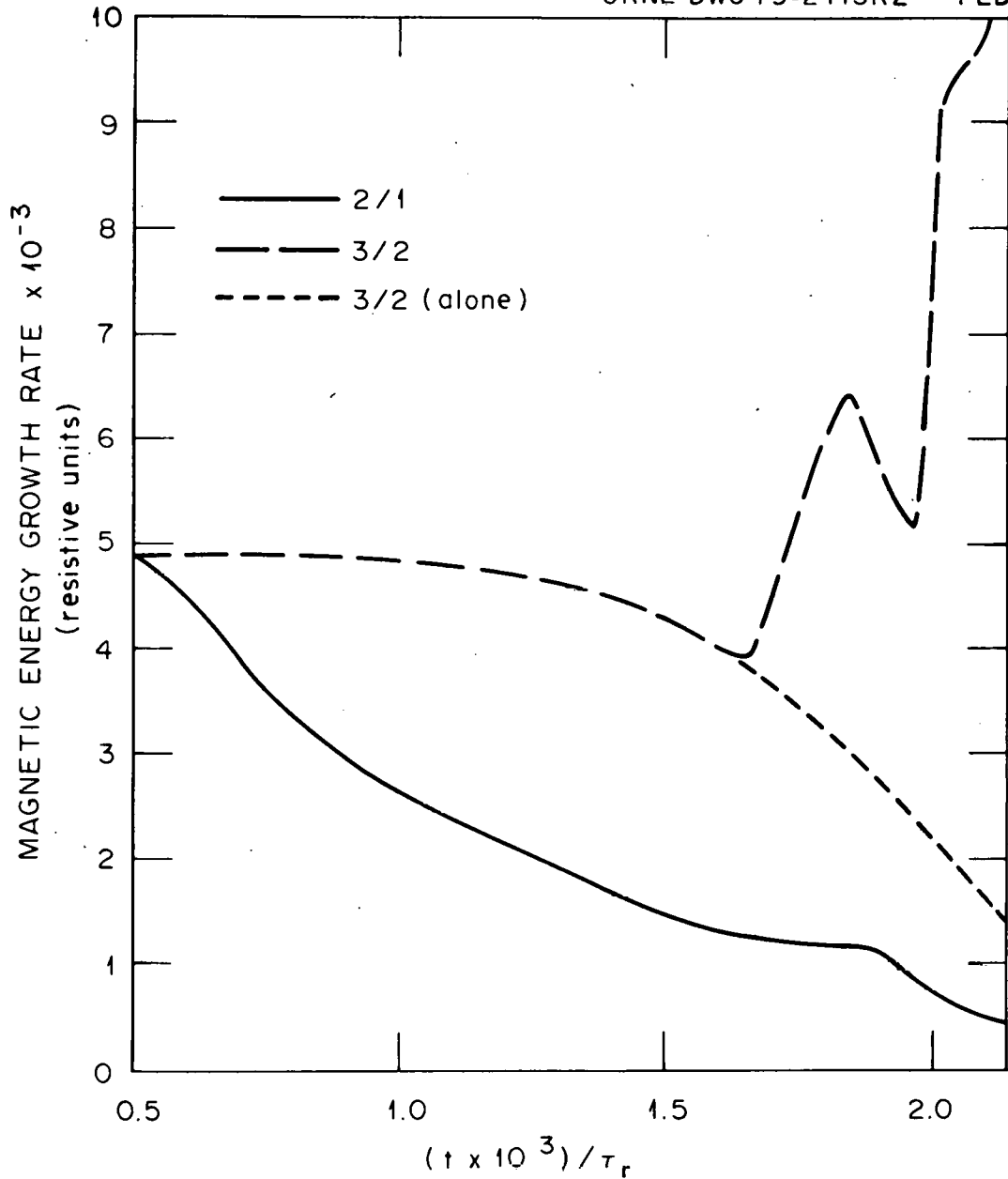


FIG. 9. Nonlinear magnetic energy growth rate of the $(m = 2; n = 1)$ mode (continuous line) and $(m = 3; n = 2)$ mode (broken line) for the same case as Fig. 8. The $(m = 3; n = 2)$ growth rate is compared with its value in the single 3/2 helicity evolution.

nonlinearly generated, and about half of the plasma radius is covered by overlapping magnetic islands, all growing significantly faster than the original linear ($m = 2; n = 1$) mode. The current density profile becomes severely deformed. This can be seen in Fig. 10, where the toroidal current density profile is plotted at the times marked by the arrows in Fig. 8. Near the end of the calculation, because of the generation of many modes, the current profile displays small scale length fluctuations. These fluctuations are not due to numerical effects. Each spike in the current covers at least ten radial grid points with no sharp discontinuities, as is shown in Fig. 11. There is a correlation between the structure in the current profile and the location of the mode-rational surfaces. That the fluctuations are not numerical has been confirmed by redoing the calculation with different time step sizes and different densities of radial grid points.

The temperature profile is also critically changed by the nonlinear interaction of the tearing modes. This profile becomes flatter in the region of island overlap, where the magnetic field lines have become stochastic. This can be seen in Fig. 12, where the electron temperature profile is shown at the same times as the current density profile. The extent of the stochastic field line region at different times can be seen in Fig. 13. To generate this figure, the magnetic field is taken at the required time, a single magnetic field line is followed several thousand times around the torus, and the intersection of this field line with the poloidal plane $\zeta = 0$ is plotted. These intersections are shown by dots in Fig. 13. Before the magnetic islands overlap, there are well-formed magnetic surfaces. In this case, all the intersection points lie on a closed line on the

ORNL-DWG 79-2560 FED

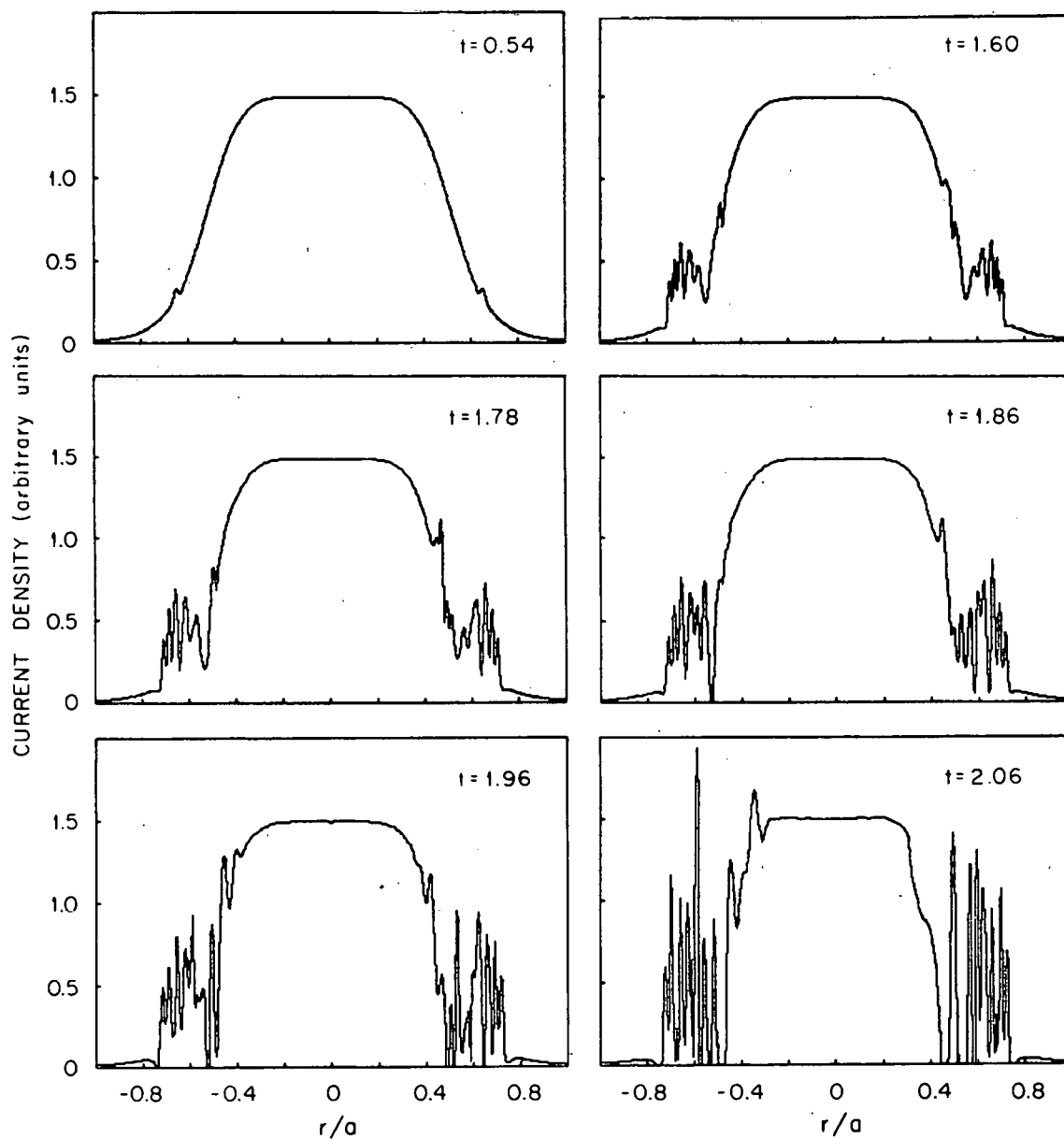


FIG. 10. Toroidal current density profile for different times during the nonlinear evolution. The time t is 10^3 times its value in resistive units. The same case is considered in Fig. 8.

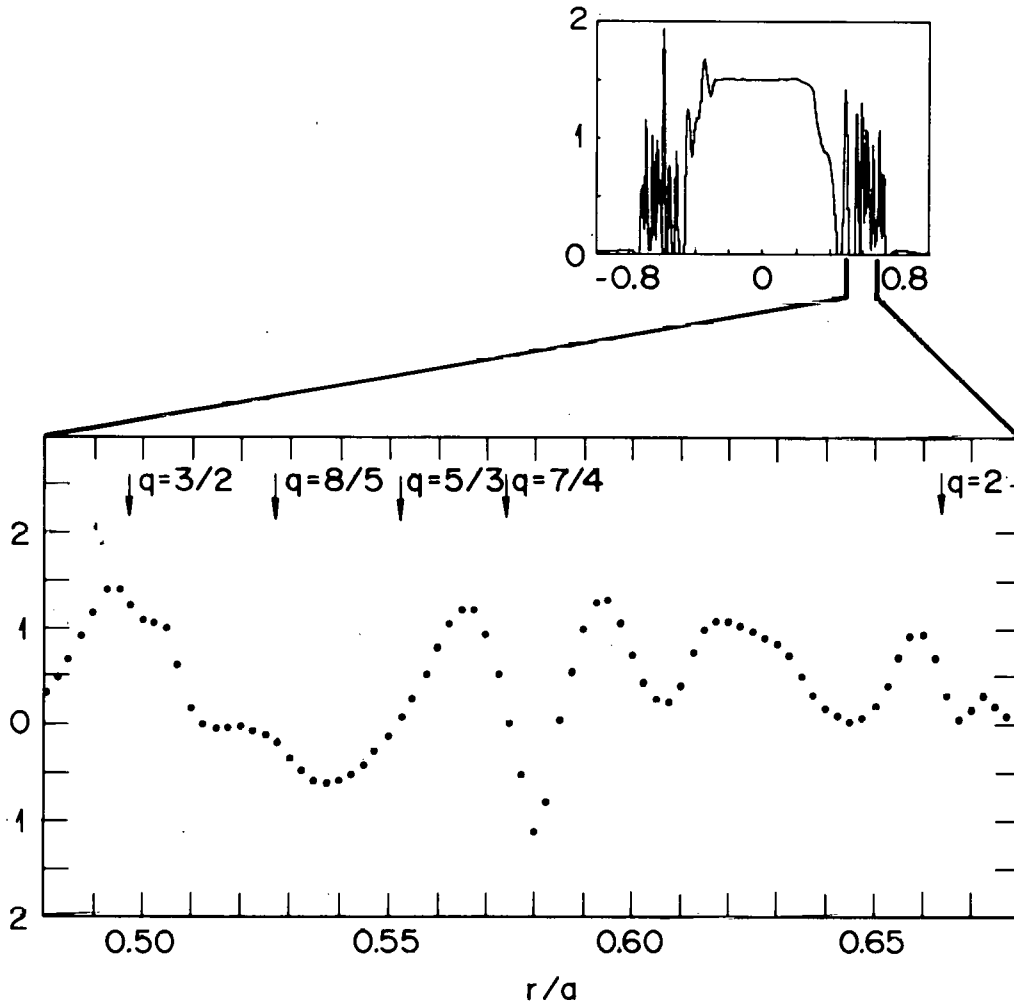


FIG. 11. Detail of the current density profile at $t = 2.06 \times 10^{-3} \tau_r$ in a radial interval $0.48 < r < 0.68$ to show the radial grid resolution. Each dot corresponds to a value of the current density at a grid point.

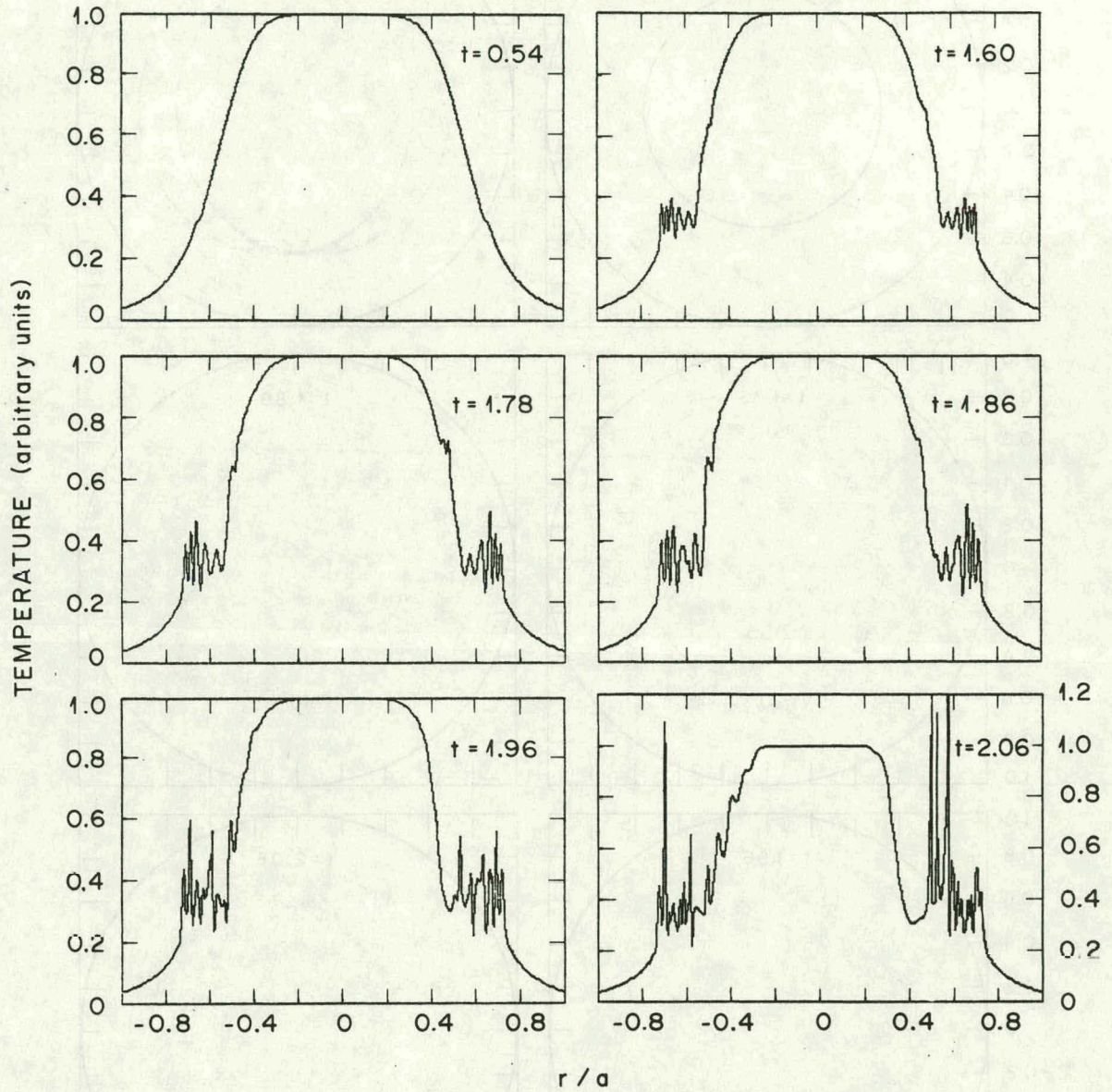


FIG. 12. Temperature profile at the times shown in Fig. 10.

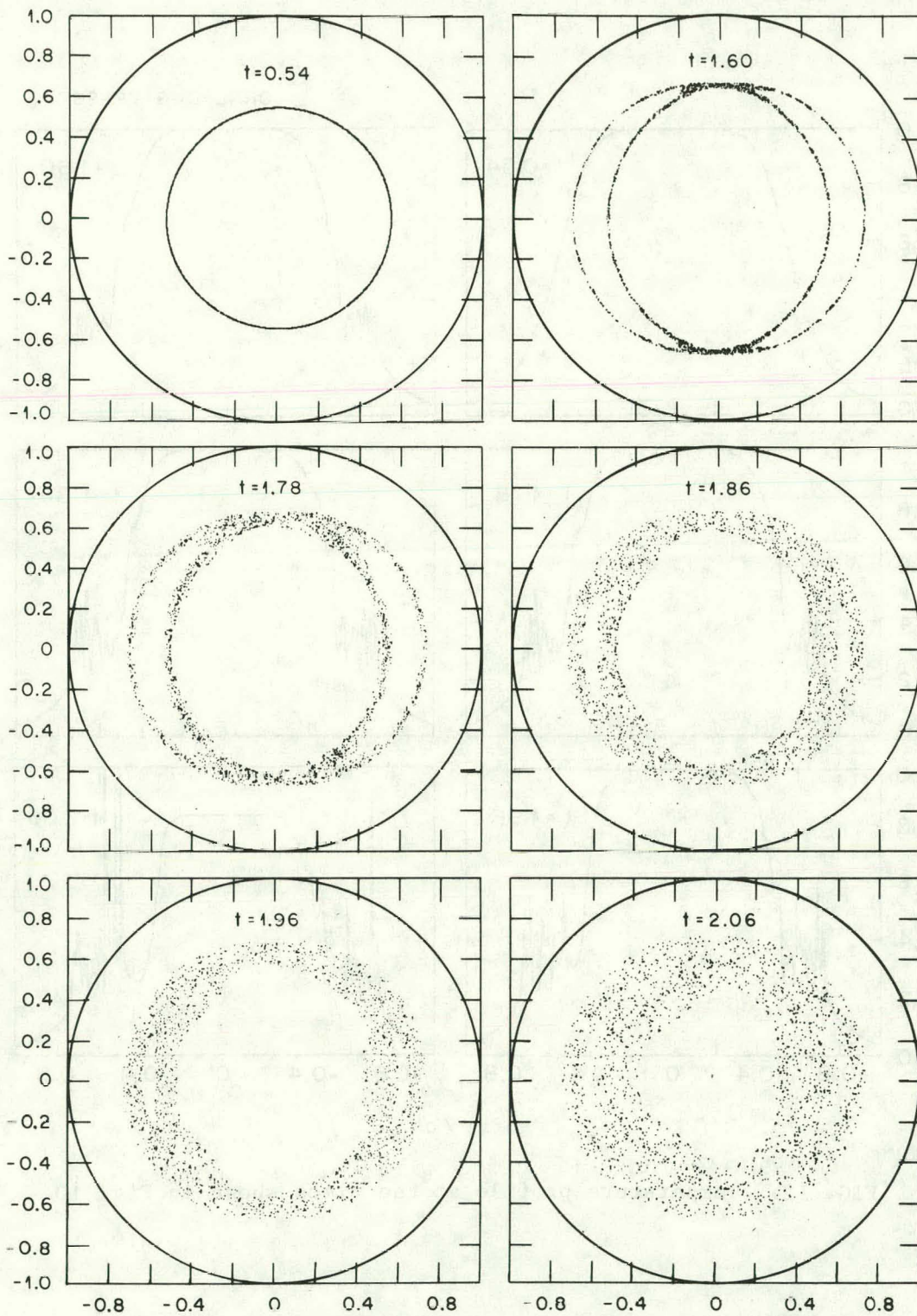


FIG. 13. Intersection of a single magnetic field line with the poloidal plane $\zeta = 0$. The field line goes through the point $r = 0.54a$, $\theta = 0$, and $\zeta = 0$. The times are the same as in Fig. 10.

poloidal plane. When magnetic surfaces are broken, the dots are scattered within a finite area, which represents the region of stochastic field lines.

When a constant current boundary condition is used during the evolution, a negative voltage spike at the wall is observed after the strong nonlinear interaction of the $(m = 2; n = 1)$ and $(m = 3; n = 2)$ tearing modes begins. The severe deformation of the current density (see Fig. 9) causes a decrease in the self-inductance of the plasma. This is the main reason for the negative voltage at the limiter. This change of voltage when the constant current boundary condition is used can be easily calculated from the conservation of energy, and it is given by

$$\Delta V = -\frac{1}{I} \frac{dE_m}{dt} - \frac{1}{I} \frac{dE_k}{dt} - \frac{\tilde{W}_J}{I}, \quad (25)$$

where E_m and E_k are the magnetic and kinetic energy, respectively; I is the total current (negative in our normalization); \tilde{W}_J is the change in the rate of energy dissipation due to Joule heating; and ΔV is the change in the voltage. The voltage is normalized to $\bar{n}B_{z0}/\mu_0$. The dominant term in the right-hand side of Eq. (25) is the first one, which gives a very fast change in voltage at the wall [see Fig. 14(a)]. This voltage change is opposite in sign from the equilibrium voltage ($V_{eq} = 9.35$ for the present equilibrium) and can be interpreted as the change in voltage generated by the change of the plasma self-inductance. When a constant voltage boundary condition is used,

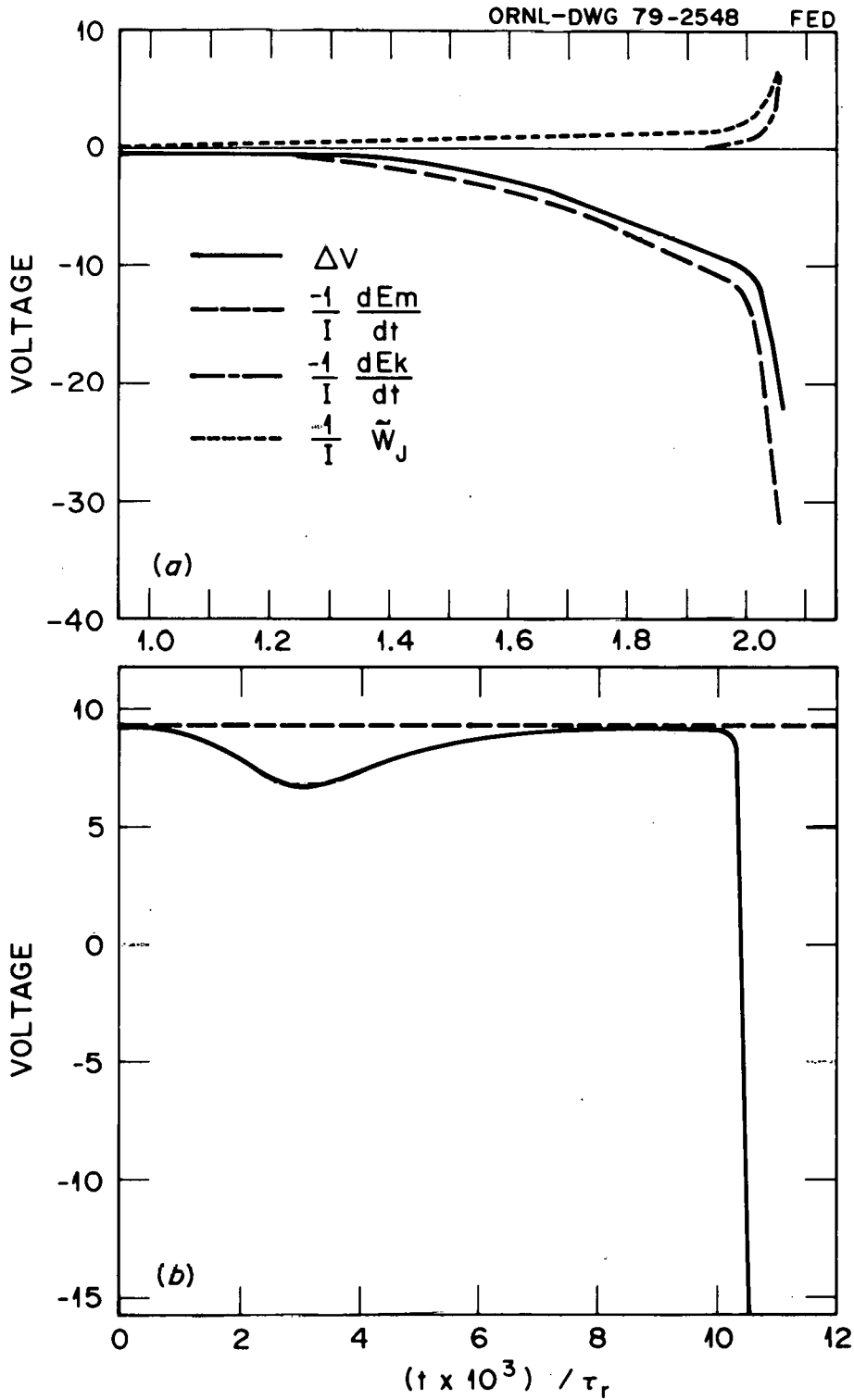


FIG. 14. Time evolution of the voltage at the limiter. The contribution from each term in Eq. (25) is indicated in the top figure. The bottom figure shows the time evolution of the voltage when the ($m = 3; n = 2$) mode is perturbed after the 2/1 magnetic island is saturated.

this effect must be inferred from the change in self-inductance in order to compare with experiment.

A case which allows a better comparison with experiment has also been numerically simulated. The only difference between these cases is that for this case only the $(m = 2; n = 1)$ mode is initially perturbed. Because the evolution is in cylindrical geometry, this mode evolves as in the single-helicity approximation, saturating with an island width $W_{21} = 0.32a$. After it is saturated, the $(m = 3; n = 2)$ mode is perturbed and the whole nonlinear evolution takes place as before. The final results are practically the same as before, but in this case the slow change in voltage at the limiter due to the $(m = 2; n = 1)$ single-helicity evolution can be contrasted to the negative voltage spike produced after the nonlinear interaction of the $(m = 2; n = 1)$ and $(m = 3; n = 2)$ modes [Fig. 14(b)]. The $(m = 2; n = 1)$ mode was perturbed at $t = 0$, and the $(m = 3; n = 2)$ mode was perturbed at $t = 0.97 \times 10^{-2} \tau_r$.

After the 2/1 and 3/2 islands overlap, the number of modes generated nonlinearly increases rapidly. Also, the magnetic energy of the higher m and n modes increases, which leads to shorter scale lengths. When these become comparable to the ion Larmor radius, the validity of a fluid picture is doubtful, and the calculation is stopped. The proliferation of higher m modes can be seen by comparing the spectrum of magnetic islands before the 2/1 and 3/2 islands overlap to the spectrum at the end of the calculation (see Fig. 15).

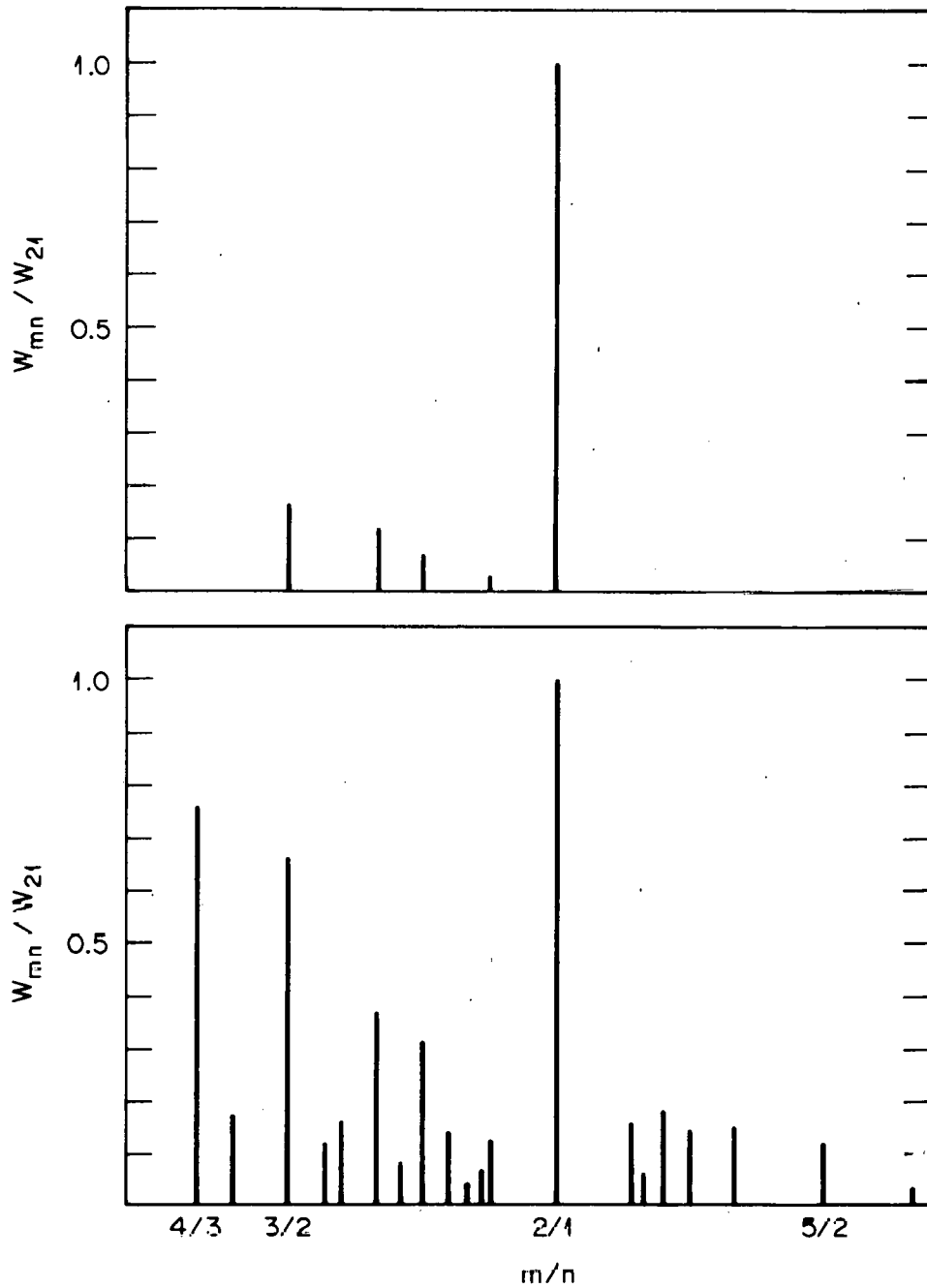


FIG. 15. Island width of the modes involved in the interaction at two different times when the $3/2$ and $2/1$ islands overlap (top) and at the end of the calculation (bottom). The island widths in both cases have been normalized to the $2/1$ island width. This is for the same calculation as presented in Fig. 8.

The nonlinear process just described does not change much when the resistivity is kept constant in time instead of being permitted to evolve. There is a slightly faster development of the nonlinear interaction when the resistivity is allowed to change in time, with values of $\bar{\chi}_{\parallel}$ and $\bar{\chi}_{\perp}$ close to the experimental values. This effect can be clearly seen in Fig. 16, which shows the plot of the time evolution of the 2/1, 3/2, and 5/3 island widths taken from two numerical calculations differing only in the way the resistivity evolves. The observed increase in speed is of the same order as the increase in linear growth rates already mentioned in Sec. III (see Fig. 5).

The perpendicular electron thermal conductivity $\bar{\chi}_{\perp}$ does not have much influence on the nonlinear process when the classical value for the perpendicular transport coefficient is used.¹⁷ Using an anomalous value for $\bar{\chi}_{\perp}$, smoother temperature profiles can be obtained during the calculation. Figure 17 compares for a fixed time the current density and temperature profiles for two different values of $\bar{\chi}_{\perp}$ ($\bar{\chi}_{\perp} = 0.05$ and $\bar{\chi}_{\perp} = 5.0$, respectively). The effect of $\bar{\chi}_{\perp}$ on the current profile is not as noticeable as it is on the temperature profile, but there is a clear tendency for the smallest scale length fluctuations in the current density profile to disappear as $\bar{\chi}_{\perp}$ is increased.

Finally, another point to consider is the effect of the initial conditions on the nonlinear evolution, i.e., the effect of changing the initial island widths $W_I^{2/1}$ and $W_I^{3/2}$ for the ($m = 2; n = 1$) and ($m = 3; n = 2$) modes, respectively. This is illustrated in Figs. 18(a) and 18(b), where the nonlinear growth rates of two modes are plotted as functions of time for different initial conditions. The nonlinear growth rate for an m/n mode is defined as

ORNL-DWG 79-2042R FED

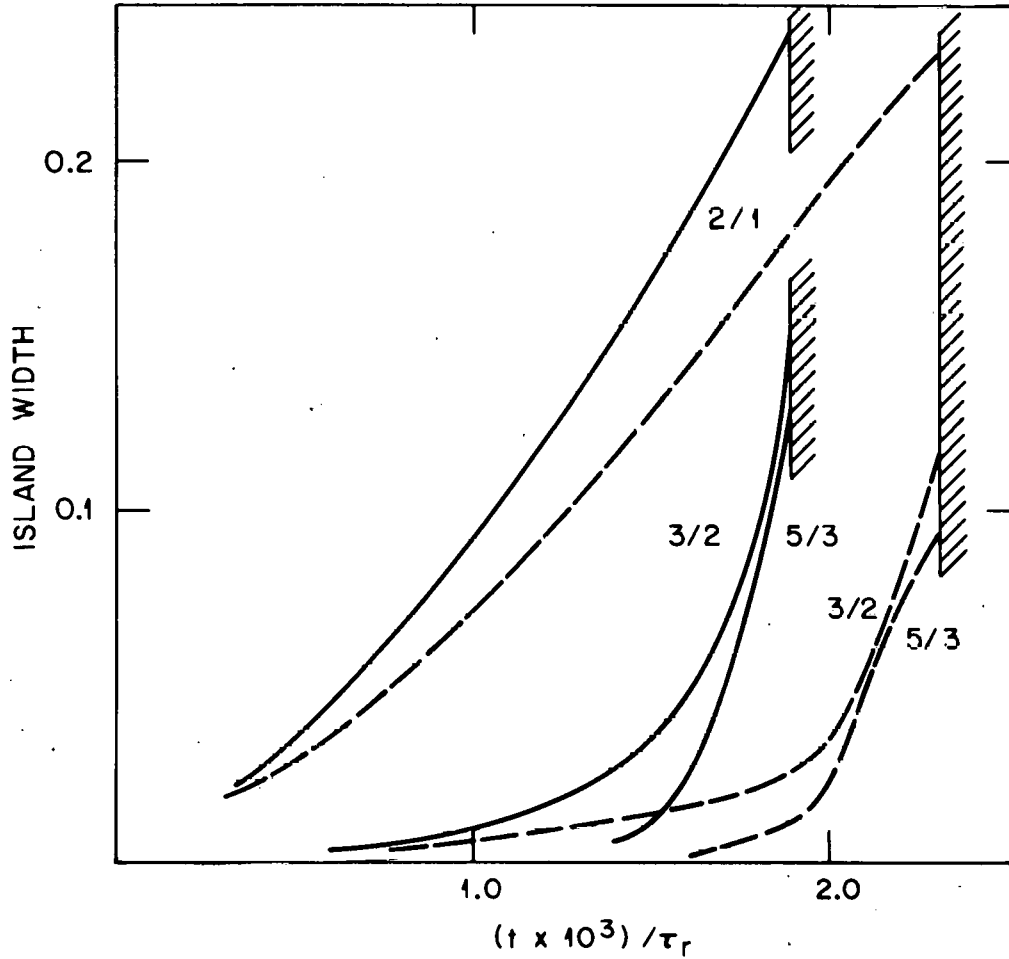


FIG. 16. Time evolution of the $(m = 2; n = 1)$, $(m = 3; n = 2)$, and $(m = 5; n = 3)$ island widths for the case considered in Fig. 8 (continuous line) compared with their evolution for time-independent resistivity (broken line).

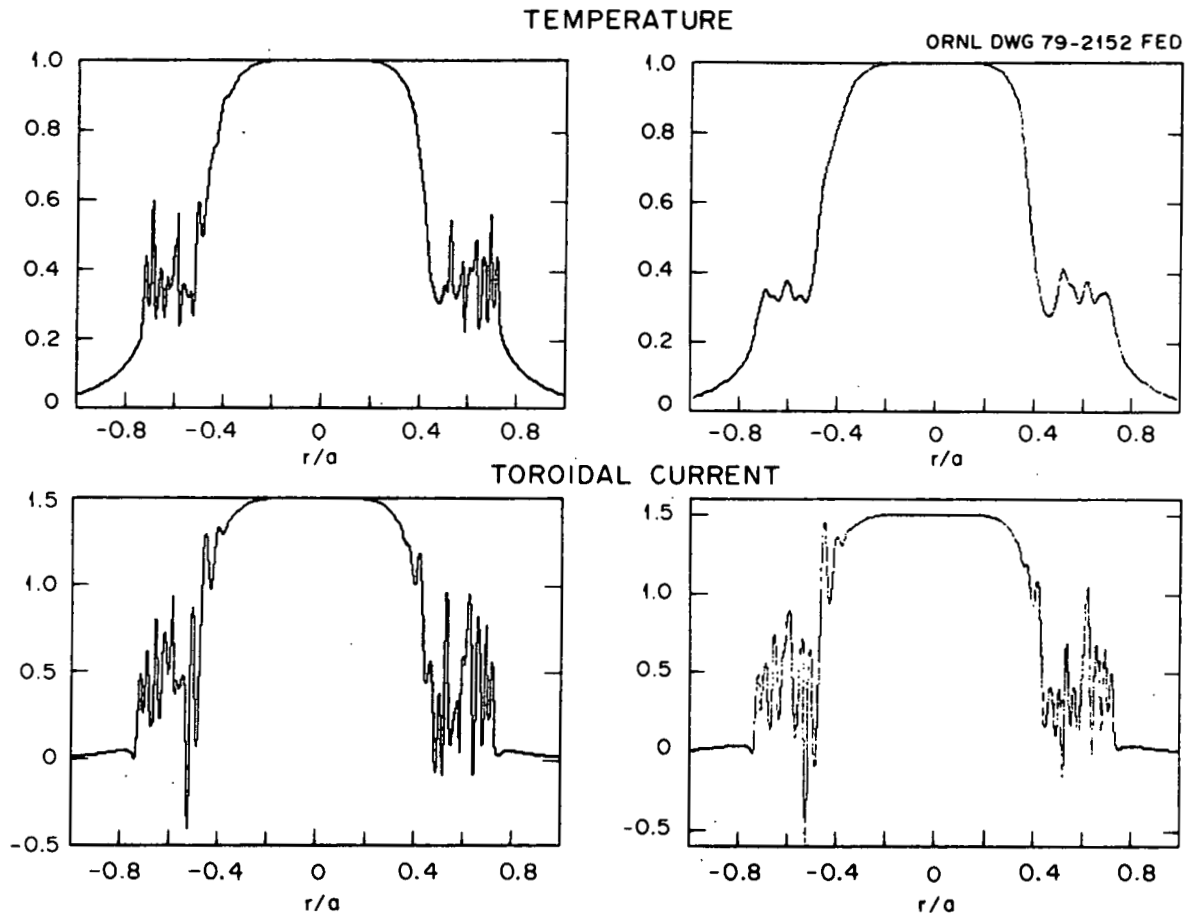


FIG. 17. Comparison of the temperature profile (top) and current density profile (bottom) between the case presented in Fig. 8 (left) and the same case with $\bar{\chi}_\perp = 5.0$ (right).

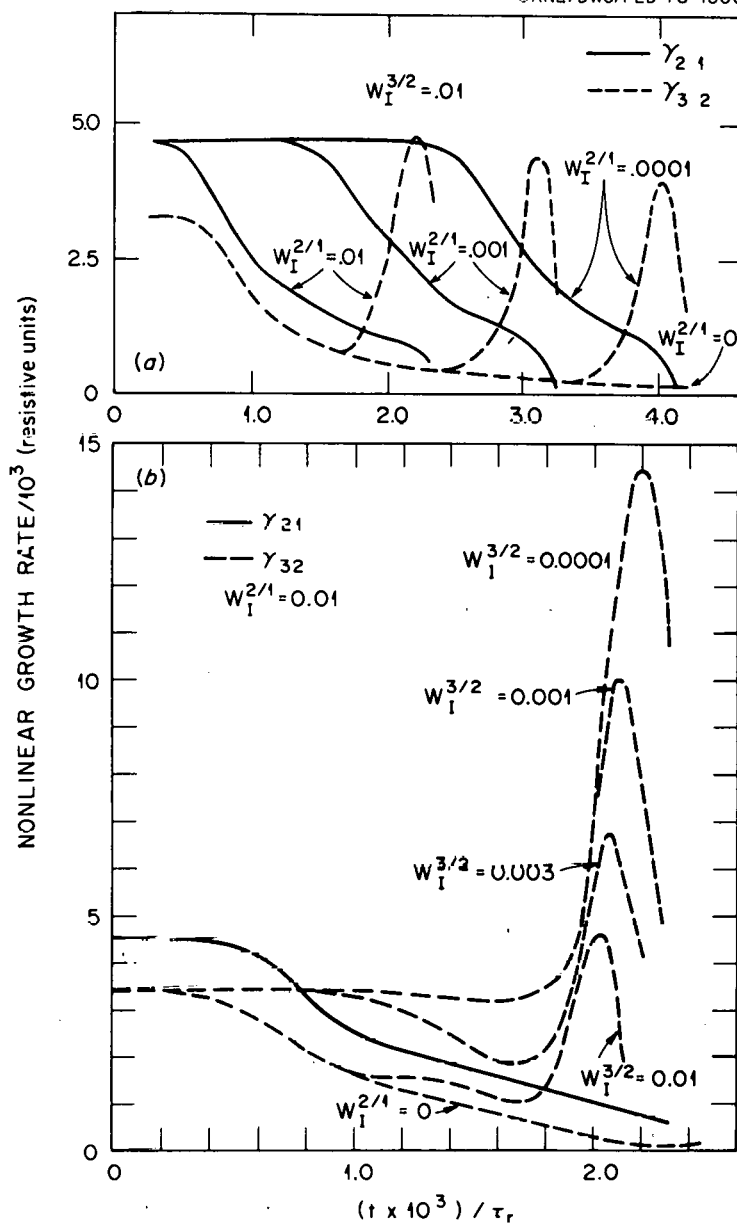


FIG. 18. Nonlinear growth rate of the ($m = 2; n = 1$) and ($m = 3; n = 2$) modes for different initial values of these perturbations: (a) the ($m = 3; n = 2$) initial perturbation is fixed with $W_I^{3/2} = 0.01a$; (b) the ($m = 2; n = 1$) initial perturbation is fixed with $W_I^{2/1} = 0.01a$. The q profile is the one considered in Sec. IV with $S = 10^6$. The resistivity is kept constant in time. In both parts of the figure, the 3/2 single-helicity result ($W_I^{2/1} = 0$) is also shown.

$$\gamma_{mn}(t) = \frac{1}{2} \frac{1}{M_{mn}} \frac{dM_{mn}}{dt}, \quad (26)$$

where M_{mn} is the magnetic energy of this mode, which in terms of the dimensionless quantities is

$$M_{mn}(t) = \pi^2 \int_0^1 r dr \left[\left(\frac{d\psi_{mn}}{dr} \right)^2 + \frac{m^2}{r^2} \psi_{mn}^2 \right]. \quad (27)$$

When the 2/1 and 3/2 islands overlap and the $(m = 3; n = 2)$ mode is strongly destabilized, $\gamma_{32}(t)$ increases and exhibits a definite peak. This diagnostic was used to detect destabilization in previous work (see Refs. 1 and 2). In Figure 18(a), $\gamma_{21}(t)$ and $\gamma_{32}(t)$ for three different initial values of $W_I^{2/1}$ have been plotted, keeping $W_I^{3/2} = 0.01a$. Decreasing $W_I^{2/1}$ delays the destabilization of the $(m = 3; n = 2)$. This results from the fact that the acceleration of this mode takes place when the islands overlap, and it takes longer for the 2/1 island to grow to the size (about $0.20a$) at which this overlap can occur. The analytic model presented in Ref. 2 to interpret the low S results predicts such a delay, and it is given by

$$\Delta t = \frac{1}{\gamma_{21}^0} \ln \left[(W_I^{2/1})' / W_I^{2/1} \right]^2, \quad (28)$$

where γ_{21}^0 is the $(m = 2; n = 1)$ linear growth rate and $(W_I^{2/1})'$ and $W_I^{2/1}$ are the initial $(m = 2; n = 1)$ island widths for two of the cases considered. For the case shown in Fig. 18(a), Eq. (28) predicts $\Delta t =$

1.023 τ_r for the time interval between two consecutive ($m = 3; n = 2$) growth rate peaks. This agrees very well with the numerical results shown in the figure. It is also important to notice that the magnetic energy of the ($m = 3; n = 2$) mode after the peak in the growth rate is the same regardless of the value of $W_I^{2/1}$. Therefore, the degree and size of the field line stochasticity region at this time are also the same.

In Fig. 18(b), $\gamma_{21}(t)$ and $\gamma_{32}(t)$ are plotted for several values of $W_I^{3/2}$ with $W_I^{2/1} = 0.01a$ fixed. As predicted by the analytical model, the position of the ($m = 3; n = 2$) peak is practically the same in all cases, and $\gamma_{21}(t)$ is totally unaffected. The different values of the height of the γ_{32} peak result in the same final magnetic energy of the ($m = 3; n = 2$) mode in all cases. It is significant also that the width of the γ_{32} peak is unchanged. Thus, the results presented in this section for a fixed equilibrium are independent of how the perturbations are initialized. The effect of changing the equilibrium q profile will be considered in the next section.

V. NONLINEAR INTERACTION OF TEARING MODES: PROFILE DEPENDENCE

The previous section concerned the nonlinear interaction of tearing modes for a particular choice of equilibrium. This interaction was particularly violent, and it led to magnetic field line stochastization in a sizable volume of the plasma. This is not generally true. This section analyzes how the interaction of tearing modes depends on the q profile.

For the present discussion, it is useful to use the parameterization of the q profile given by Eq. (21). The results of the nonlinear evolution of tearing modes will be described as a function of $q(0)$ and the parameter λ . Throughout this section, $q_0 = 4.1$ unless otherwise stated. When $q(0)$ is between 1 and 1.5, only the $(m = 2; n = 1)$ and $(m = 3; n = 2)$ tearing modes can be linearly unstable. Thus, only these two modes are initially perturbed in our calculations. The results of the nonlinear evolution do not depend on the size of these initial perturbations, as has been seen in Sec. IV. Therefore, all the calculations presented in this section are based on the same initial magnetic island widths of these perturbations ($W_I^{3/2} = W_I^{2/1} = 0.01a$).

The equilibria considered can be classified in three groups. The criterion for this classification is the nonlinear behavior of the $(m = 3; n = 2)$ mode. The first group includes equilibrium profiles for which the $(m = 3; n = 2)$ mode is either stable or has nonlinear growth which is not affected by the evolution of the $(m = 2; n = 1)$ mode. For such cases, the $(m = 3; n = 2)$ mode saturates at very low level, $W_{32} < 0.05a$, and in practice only the 2/1 magnetic island is detectable. That happens in general for $1 < \lambda < 2$ (region I in Fig. 19). If λ is

ORNL DWG 2874 FED

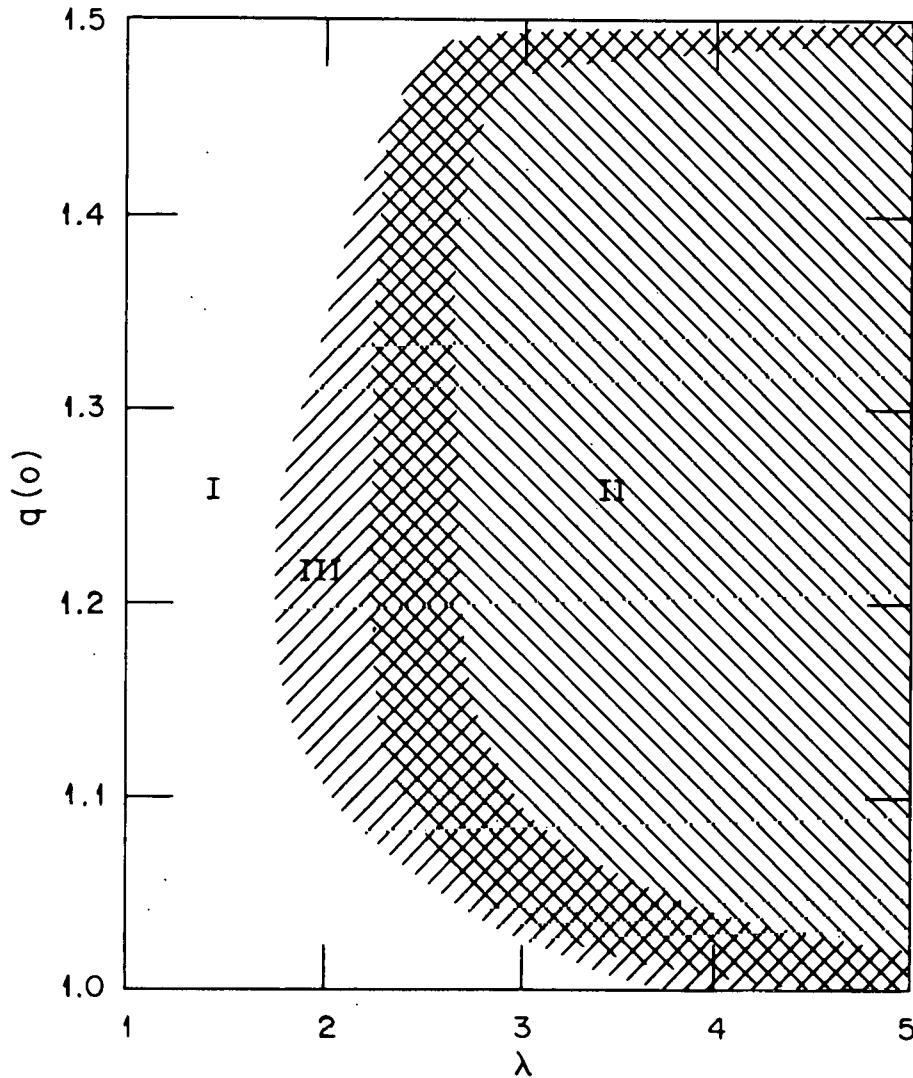


FIG. 19. Nonlinear stability regions in the $\lambda - q(0)$ plane: I — the $(m = 3; n = 2)$ mode is stable; II — the $(m = 2; n = 1)$ interacts strongly with the $(m = 3; n = 2)$, mode coupling being the dominant mechanism; III — the $(m = 3; n = 2)$ is mainly destabilized by the $(m = 2; n = 1)$ through the modification of the equilibrium current profile.

close to 1 and $q(0)$ is also near 1, the $(m = 2; n = 1)$ mode is also stable.

The second group of profiles is characterized by the $(m = 3; n = 2)$ mode being strongly destabilized during its evolution by the $(m = 2; n = 1)$ on a very short time scale. A typical example is the case described in the previous section. The equilibrium q profiles for these cases are characterized by $\lambda > 2.5$ and $q(0) > 1$ (region II in Fig. 19). The destabilization of the $(m = 3; n = 2)$ mode will be shown to be mainly due to the coupling to the $(m = 2; n = 1)$ mode through the $(m = 5; n = 3)$ and $(m = 1; n = 1)$ modes, rather than through the $(m = 0; n = 0)$ mode.

Finally, the third group includes cases that are between the other two groups. The $(m = 3; n = 2)$ is destabilized on a slow time scale, the destabilization essentially resulting from the deformation of the equilibrium current by the $(m = 2; n = 1)$ mode. This corresponds to a narrow range of values for the parameter λ , as can be seen in Fig. 19, region III. There is not a well-defined boundary between the three regions.

In classifying the results of the calculations, it is necessary to analyze them carefully. As a diagnostic for the destabilization of the $(m = 3; n = 2)$ mode, the nonlinear growth rate of the magnetic energy of this mode, $\gamma_{32}(t)$, is used. Using $\gamma_{32}(t)$ allows a simple analysis of the results and makes comparison with the analytic model presented in Refs. 1 and 2 easy. The present analysis will be limited to the first phase of destabilization, lasting up to the peak of the $(m = 3; n = 2)$ nonlinear growth rate. The reason is that only a few modes are involved at this time, which allows the analytic model^{1,2} to be used to

interpret the results. After that, when the growth rates increase very rapidly (see Fig. 9), many modes are involved and the model is no longer valid.

To distinguish the cases in which the dominant destabilization mechanism is mode coupling from the cases in which the destabilization is mainly due to the deformation of the current profile (quasi-linear effect), the RSF code has been a useful tool. This code permits inclusion or suppression, at will, of individual modes in the nonlinear evolution. A quasi-linear case can be run; it is analogous to the one discussed in Sec. IV but includes only the $m/n = 2$ and $m/n = 3/2$ helicities. In this way, there is no possibility of a direct coupling between the two helicities, and each is aware of the other only through the deformation of the equilibrium profile. Figure 20(a) shows that in region II, the deformation of the equilibrium current does not explain the $(m = 3; n = 2)$ destabilization. However, the opposite result is obtained if the equilibrium q profile belongs to region III, as shown in Fig. 20(b).

Such cases can be further analyzed by subtracting the quasi-linear contribution [the broken line in Fig. 20(a)] from the full nonlinear growth rate of the $(m = 3; n = 2)$ mode [the continuous line in Fig. 20(a)]; the resulting function $\tilde{\gamma}_{32}(t)$ gives a measure of the destabilization due to mode coupling. In Fig. 21, $\tilde{\gamma}_{32}(t)$ is plotted for four different profiles, with $q(0) = 1.08$; $q_0 = 4.1$, and $\lambda = 2.25, 2.5, 3, \text{ and } 3.5$, respectively. To show the correlation between the overlap of the 2/1 and 3/2 magnetic islands and the beginning of the destabilization of the $(m = 3; n = 2)$ mode, the time when the islands touch in each case is marked with an arrow in Fig. 21. For $\lambda > 3.0$,

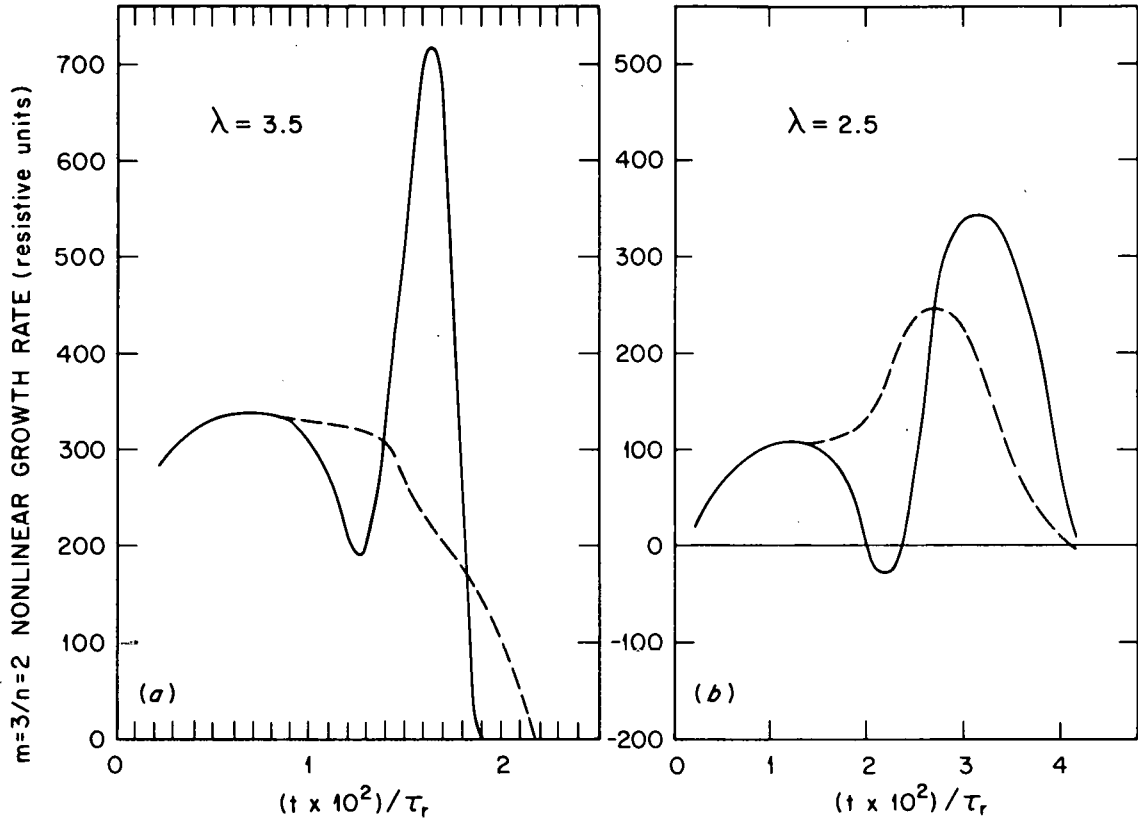


FIG. 20. Time evolution of the nonlinear growth rate of the ($m = 3; n = 2$) mode exhibiting the peak due to the destabilization by the ($m = 2; n = 1$) mode (continuous line). The case in which only the 2/1 and 3/2 helicities are included in the calculation corresponds to the broken line. The equilibrium profiles are given by Eq. (21), with $q(0) = 1.08$, $q_L = 4.2$, and $\lambda = 3.5$ (a) and 2.5(b), respectively.

ORNL-DWG 79-2558 FED

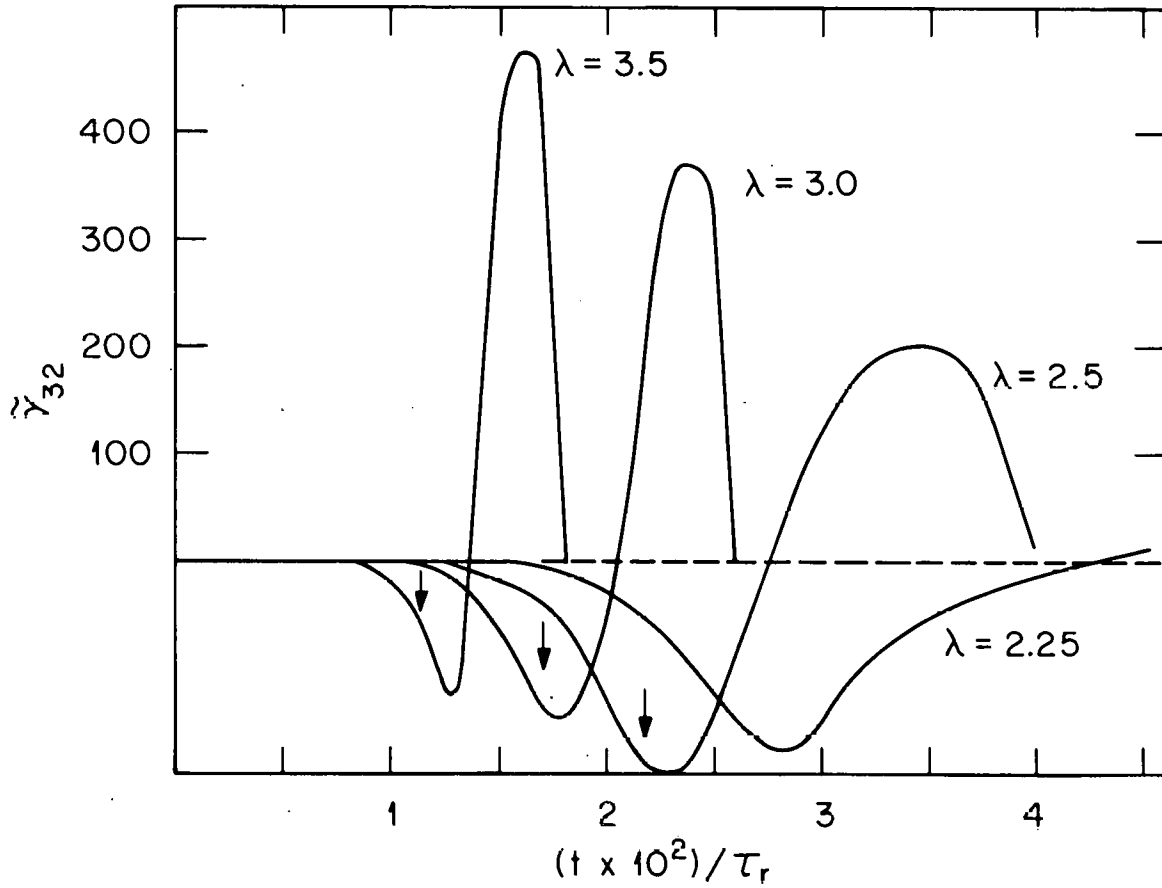


FIG. 21. The contribution to the peak of the ($m = 3; n = 2$) nonlinear growth rate due to mode coupling. The equilibrium q profiles are given by Eq. (21), with $q(0) = 1.08$, $q_0 = 4$.

there is a clear destabilizing effect due to mode coupling. This is characterized by the quantity

$$g \equiv \int \gamma_{32}(t) dt$$

being positive. The case with $\lambda = 2.5$ is borderline, where $g \approx 0$. For this case, the quasi-linear destabilization dominates. Finally, for $\lambda = 2.25$ the mode coupling has, if anything, a stabilizing effect, but in practice the $(m = 3; n = 2)$ mode is not significantly affected by the evolution of the $(m = 2; n = 1)$ mode.

In Ref. 4, an analytic model was developed to clarify the main features of the strong destabilization of the $(m = 3; n = 2)$ mode by the $(m = 2; n = 1)$ mode. The main assumption of the model is that only the nonlinear coupling of five tearing modes $(m = 2; n = 1)$, $(m = 3; n = 2)$, $(m = 5; n = 3)$, $(m = 1; n = 1)$, and $(m = 0; n = 0)$ is required. This assumption has been fully tested with the RSF code. In Fig. 22, $\gamma_{32}(t)$ is compared for three cases: one with five modes, one with 29 modes, and the single-helicity case. The main features of the $(m = 3; n = 2)$ destabilization are present even in the five mode run. However, this run fails to give an accurate description of the last part of the evolution, in which a stochastic region has been generated. As is shown in Fig. 15, these final stages of the calculation require a large number of modes. The results in Fig. 22 are for the q profile and parameters discussed in Sec. IV, except that the evolution of the resistivity is not included.

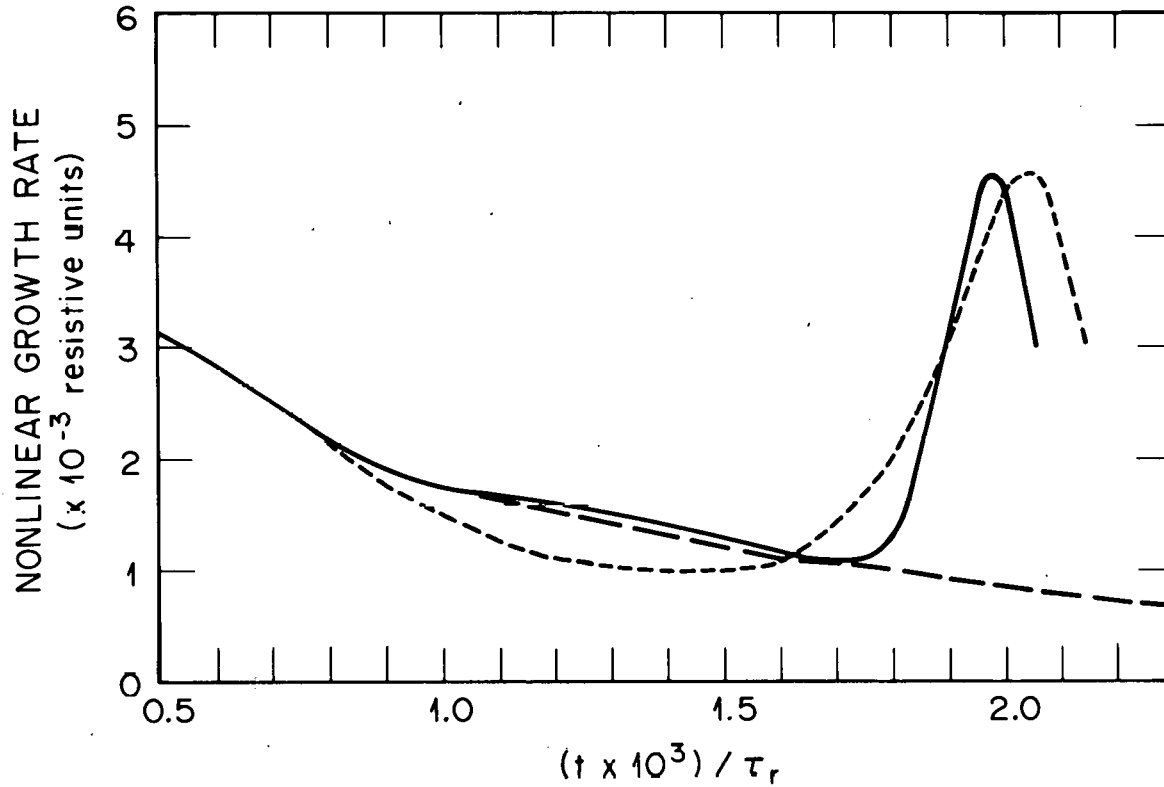


FIG. 22. Nonlinear growth rate of the $(m = 3; n = 2)$ mode for a calculation in which 5 modes were included (----) compared with the same case with 29 modes included (——). Finally, it is also compared with the case in which only the 3/2 helicity is included in the calculation (— — —).

One of the predictions of the analytic model is that the width Γ of the peak of the $(m = 3; n = 2)$ nonlinear growth rate is

$$\Gamma = (\sqrt{2})/\gamma_{21}^0, \quad (29)$$

where γ_{21}^0 is the linear growth rate of the $(m = 2; n = 1)$ mode. For $S = 2 \times 10^4$, 13 different q profiles for which the $(m = 3; n = 2)$ is strongly destabilized have been studied. For each case, Γ was calculated as the width of the $\gamma_{32}(t)$ peak at half of its maximum value. The mean value of $\Gamma \gamma_{21}^0$ for all these cases is 1.44, the standard deviation being 0.16. Although this model was derived for low S , the numerical results indicate that the relation in Eq. (29) holds for higher values of S , as can be seen in Fig. 23.

Equilibria that cannot be characterized by the simple parameterization given by Eq. (21) have also been studied. The main problem with the parameterization of Eq. (21) is that a single parameter λ controls the flattening of the profile near the magnetic axis, the slope of the equilibrium current near the singular surface, and the value of the resistivity at this point. To decouple the shaping of the profile near the singular surface from the behavior near the magnetic axis, λ can be made functionally dependent on r . This allows more flexibility but makes a parametric study of the stability properties more difficult. The result is that the high gradients near the singular surfaces of the $(m = 2; n = 1)$ and $(m = 3; n = 2)$ modes, more than the flattening near the magnetic axis, makes the interaction strong between these two modes. In general, it can be concluded that the interaction between the two modes will be very strong if, in the

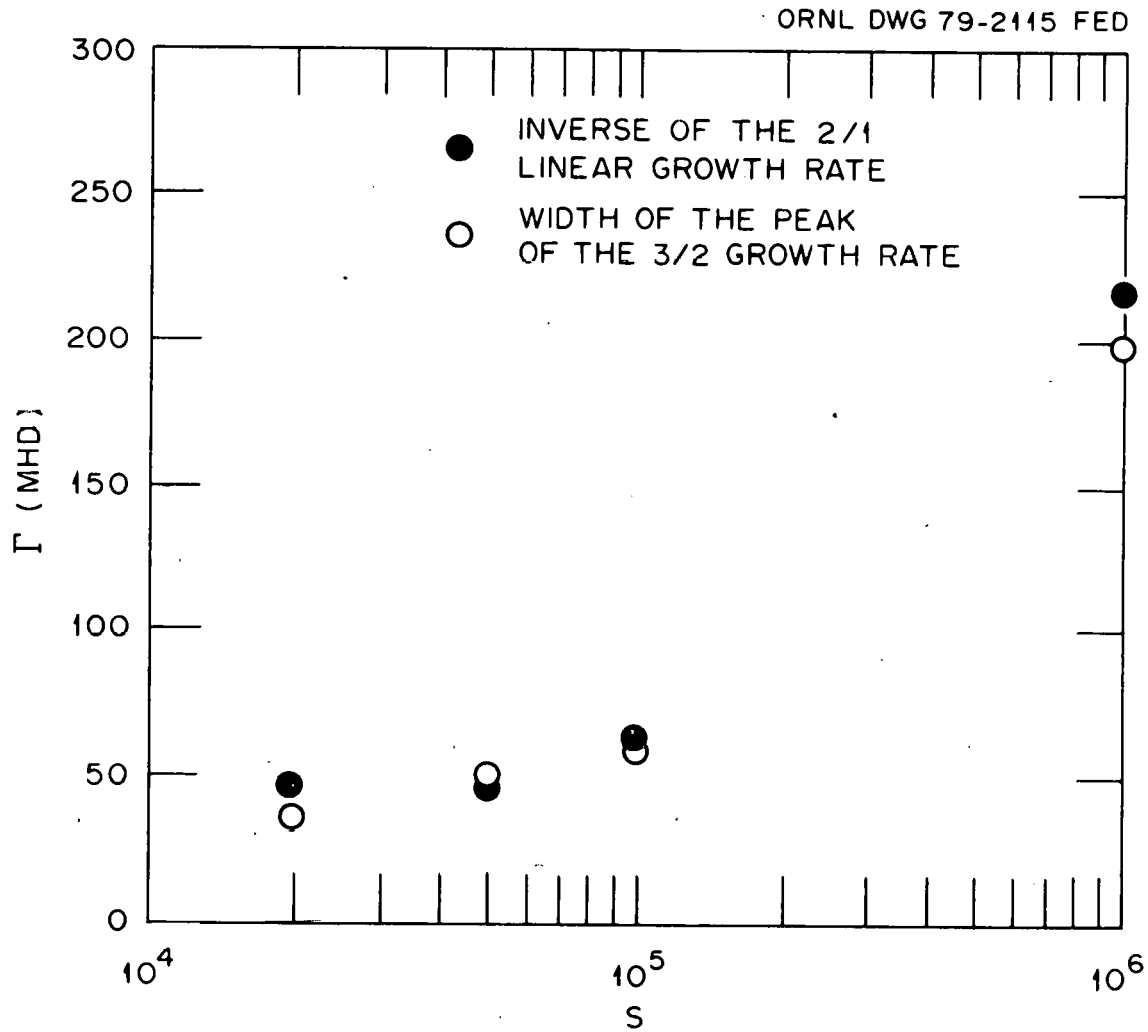


FIG. 23. The width of the peak of the ($m = 3; n = 2$) nonlinear growth rate for different values of S . This is compared with the inverse of the ($m = 2; n = 1$) linear growth rate. The calculations were done for the q profile discussed in Sec. IV.

nonlinear evolution, the magnetic islands associated with them can overlap, that is, if

$$r_{21} - r_{32} < \frac{1}{2}(W_{21} + W_{32}),$$

where r_{mn} is the position of the singular surface for the (m;n) mode and W_{mn} is its saturated island width in the single-helicity approximation.

VI. COMPARISON WITH EXPERIMENT

Many of the features of the strong nonlinear interaction of tearing modes described in preceding sections are similar to the characteristic features of a tokamak disruption. The detailed calculations presented in this paper give stronger support to the suggestion¹ that this interaction is the dynamical mechanism responsible for some tokamak disruptions. If the width of the peak of the $(m = 3; n = 2)$ growth rate Γ is identified with the characteristic time scale for the nonlinear process, then Γ can be compared with the experimental disruption time, taken to be the width of the voltage spike. As previously reported,¹⁸ this comparison was favorable when extrapolated from low S results. The present results confirm that even at large S , Γ is of the order of the inverse of the $(m = 2; n = 1)$ linear growth rate (Fig. 23). This type of scaling agrees with the experimental disruption time for present-day tokamaks.¹⁸

A more detailed comparison of the present results with experiment would require knowledge of the experimental current density profile prior to a major disruption and of the mode structure before and during a major tokamak disruption. In a few cases, some indirect knowledge of the current density profile can be gained through the measurement of the electron temperature profile.^{4,5} Also, there is ample experimental evidence of the presence of a $(m = 2; n = 1)$ mode before major disruptions. However, no details are known about the modes involved during the disruption. Thus, only a partial comparison can be made with experiment.

Two cases in which there is detailed measurement of the electron temperature profile before a major disruption will be considered. The first case corresponds to a major disruption in the PLT tokamak.⁴ The equilibrium q profile considered in Sec. IV was obtained from the electron temperature profile measured in this case. The values of the parameters $S = 10^6$, $\bar{\chi}_{\parallel} = 10^7$, and $\bar{\chi}_{\perp} = 0.05$ are close to the values for this experiment ($S = 10^7$, $\bar{\chi}_{\parallel} = 10^8$, and $\bar{\chi}_{\perp} = 0.005$). The results of the calculation show agreement with the experimental observations: poloidal asymmetry due to the presence of the odd m modes and the right order of magnitude for the time scale of the process ($\Gamma = 200 \tau_{hp}$). However, no experimental information exists on the mode number of the odd component observed during the disruption, making a complete comparison impossible. The second case considered is a major disruption produced in the Impurity Study Experiment (ISX-A) tokamak by a deliberate tungsten injection. Here, an electron temperature profile measurement was obtained prior to the major disruption.⁵ This electron temperature profile [as well as the toroidal current, see Fig. (24)] is slightly hollow, but this hollowness is not essential for the results obtained. The $(m = 2; n = 1)$ and $(m = 3; n = 2)$ modes are linearly unstable, and their nonlinear evolution is similar to that of the previous case. The results for this case have been summarized in Fig. 24, which shows the time evolution of the magnetic islands and the voltage at the limiter. In this case, experimental information on the magnetohydrodynamic modes during the disruption is also lacking.

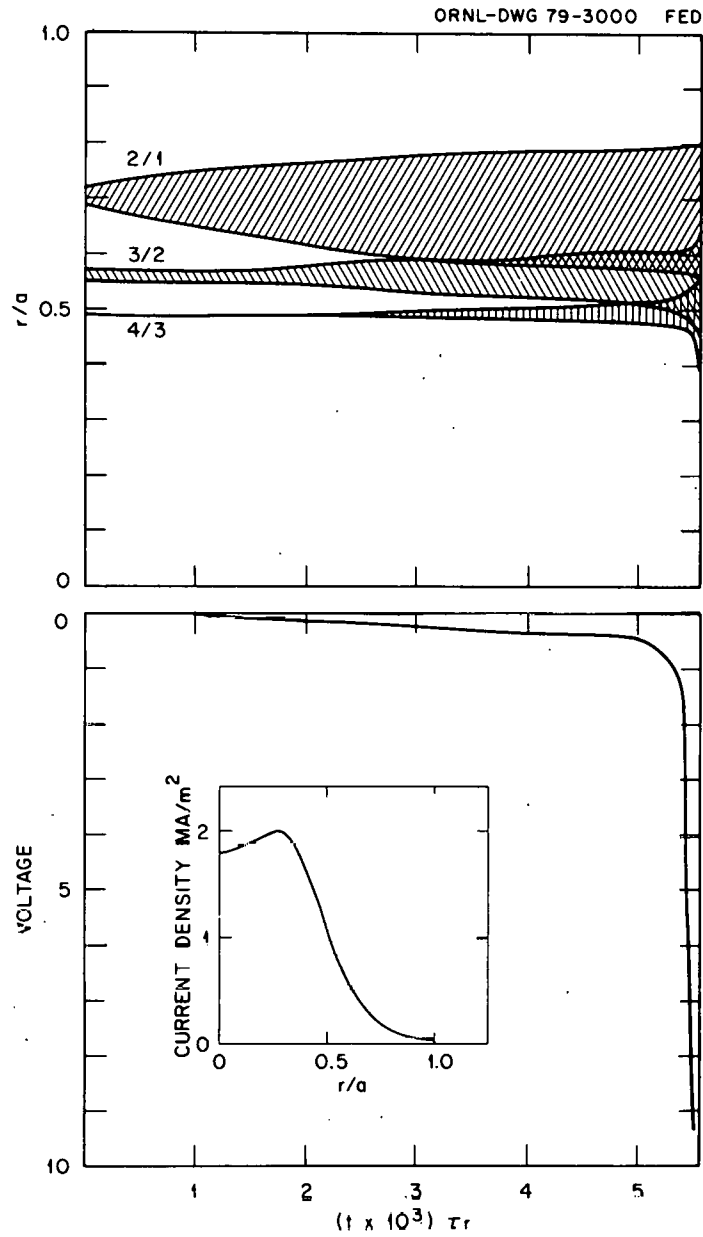


FIG. 24. Nonlinear evolution of the 2/1 and 3/2 magnetic islands (top) and change of the voltage at the limiter (bottom) for a current density profile (insert) prior to a major disruption in the ISX-A tokamak.

VII. CONCLUSIONS

The results presented here indicate the following:

(i) The nonlinear destabilization of the $(m = 3; n = 2)$ mode by the $(m = 2; n = 1)$ mode has been confirmed for a wide set of equilibria. There is now clear evidence of this effect and of its consequences (generation of many islands of different helicities, field line stochastization in a sizable plasma volume, and negative voltage spike at the limiter).

(ii) The time scale for this process is of the order of $(\gamma_{21}^0)^{-1}$, but its precise value depends on details of the dynamics such as temperature effects. This time scale holds even at large S (10^6).

(iii) This mechanism could be responsible for major disruptions in tokamaks. It appears to be consistent with present experimental data. However, to confirm this mechanism to the exclusion of others, more experimental information is necessary, particularly on the magnetohydrodynamic modes involved in the disruption.

Finally, it should be noted that for a more complete understanding of the nonlinear interaction of tearing modes in tokamaks, it is necessary to incorporate toroidal and finite β effects. This effort is currently under way.

THIS PAGE
WAS INTENTIONALLY
LEFT BLANK

ACKNOWLEDGMENTS

The authors would like to thank M. Murakami for the Thomson scattering profiles⁵ obtained from ISX-A. The authors are also indebted to J. D. Callen for encouragement and discussions during the course of this work.

This research was sponsored by the Office of Fusion Energy, U. S. Department of Energy, under contract W-7405-eng-26 with the Union Carbide Corporation.

REFERENCES

- ¹B. V. Waddell, B. Carreras, H. R. Hicks, J. A. Holmes, and D. K. Lee, Phys. Rev. Lett. 41, 1386 (1978).
- ²B. V. Waddell, B. Carreras, H. R. Hicks, and J. A. Holmes, Phys. Fluids 22, 896 (1979).
- ³H. R. Hicks, B. Carreras, J. A. Holmes, D. K. Lee, and B. V. Waddell, Oak Ridge National Laboratory Report ORNL/TM-7132, Oak Ridge, Tennessee (1979).
- ⁴N. R. Sauthoff, S. von Goeler, and W. Stodiek, Nucl. Fusion 18, 1445 (1978).
- ⁵M. Murakami, K. H. Burrell, T. C. Jernigan, T. Amano, S. C. Bates, C. E. Bush, R. E. Clausing, R. J. Colchin, E. C. Crume, Jr., J. C. DeBoo, J. L. Dunlap, G. R. Dyer, P. H. Edmonds, L. C. Emerson, A. C. England, E. S. Ensberg, C. A. Foster, Y. Gomag, K. W. Hill, H. C. Howe, R. C. Isler, H. E. Ketterer, P. W. King, R. A. Langley, J. F. Lyon, D. H. McNeill, J. T. Mihalczko, S. L. Milora, W. Namkung, A. P. Navarro, R. V. Neidigh, G. H. Neilson, V. K. Paré, R. Prater, M. J. Saltmarsh, M. J. Schaffer, J. E. Simpkins, D. W. Swain, J. B. Wilgen, W. R. Wing, S. K. Wong, B. Zurro, in Plasma Physics and Controlled Nuclear Fusion Research (International Atomic Energy Agency, 1979), Vol. I, p. 269; M. Murakami (Oak Ridge National Laboratory), private communication, 1978.

- ⁶P. H. Rutherford, Phys. Fluids 16, 1903 (1973).
- ⁷M. N. Bussac, D. Edery, R. Pellat, and J. L. Soule, in Plasma Physics and Controlled Nuclear Fusion Research (International Atomic Energy Agency, Vienna, 1977), Vol. I, p. 607.
- ⁸H. R. Strauss, Phys. Fluids 19, 134 (1976).
- ⁹M. N. Rosenbluth, D. A. Monticello, H. Strauss, and R. B. White, Phys. Fluids 19, 1987 (1976).
- ¹⁰H. Welter and D. Biskamp, Bull. Am. Phys. Soc. 23, 872 (1978).
- ¹¹H. P. Furth, P. H. Rutherford, and H. Selberg, Phys. Fluids 16, 1054 (1973).
- ¹²H. P. Furth, in Propagation and Instabilities in Plasmas, ed. by W. I. Fetterman (Stanford University Press, Stanford, California, 1973), p. 87.
- ¹³R. B. White, D. A. Monticello, M. N. Rosenbluth, and B. V. Waddell, Phys. Fluids 20, 800 (1977).
- ¹⁴B. Carreras, B. V. Waddell, and H. R. Hicks, Oak Ridge National Laboratory Report ORNL/TM-6403, Oak Ridge, Tennessee (1978).

- ¹⁵R. B. White, D. A. Monticello, and M. N. Rosenbluth, *Phys. Rev. Lett.* 39, 1678 (1977).
- ¹⁶D. Biskamp and H. Welter, in Plasma Physics and Controlled Nuclear Fusion Research (International Atomic Energy Agency, Vienna, 1977), Vol. I, p. 579.
- ¹⁷S. I. Braginskii, in Reviews of Plasma Physics, ed. by M. A. Levisovich (Consultants Bureau, New York, 1965), Vol. I, p. 205.
- ¹⁸J. D. Callen, B. V. Waddell, B. Carreras, M. Azumi, P. J. Catto, H. R. Hicks, J. A. Holmes, D. K. Lee, S. J. Lynch, J. Smith, M. Soler, K. T. Tsang, J. C. Whitson, in Plasma Physics and Controlled Nuclear Fusion Research (International Atomic Energy Agency, Vienna, 1979), Vol. I, p. 415.

**THIS PAGE
WAS INTENTIONALLY
LEFT BLANK**

INTERNAL DISTRIBUTION

- | | |
|------------------|---|
| 1. B. Carreras | 15. S. Yokosawa |
| 2. R. A. Dory | 16-17. Laboratory Records Department |
| 3. J. Dunlap | 18. Laboratory Records, ORNL-RC |
| 4-9. H. R. Hicks | 19. Document Reference Section |
| 10. J. T. Hogan | 20-21. Central Research Library |
| 11. J. A. Holmes | 22. Fusion Energy Division Library |
| 12. M. Peng | 23. Fusion Energy Division
Communications Center |
| 13. J. Sheffield | 24. ORNL Patent Office |
| 14. D. J. Sigmar | |

EXTERNAL DISTRIBUTION

25. D. J. Anthony, Energy Systems and Technology Division, General Electric Company, 1 River Road, Bldg. 23, Room 290, Schenectady, NY 12345
26. Bibliothek, Institute for Plasma Physics, 8046 Garching bei München, Federal Republic of Germany
27. Bibliothèque, Service du Confinement des Plasmas, C.E.A., B.P. No. 6, 92, Fontenay-aux-Roses (Seine), France
28. D. Biskamp, Max Planck Institut für Plasmaphysik, D-8046 Garching bei München, Federal Republic of Germany
29. J. V. Brackbill, CTR-6, MS642, Los Alamos, NM 87544
30. J. D. Callen, Nuclear Engineering Department, University of Wisconsin, Engineering Research Building, 1500 Johnson Drive, Madison, WI 53706
31. L. Cheung, Department of Electronics, University Science Center, The Chinese University of Hong Kong, Shatin, N.T., Hong Kong
32. F. F. Cap, A 6020 Innsbruck, Innerebnerstr 40, Austria, Europe
33. J. F. Clarke, Office of Fusion Energy, G-234, Department of Energy, Washington, DC 20545
34. R. W. Conn, Fusion Technology Program, Nuclear Engineering Department, University of Wisconsin, Madison, WI 53706
35. CTR Library, c/o A. F. Haught, United Technologies Research Laboratory, East Hartford, CT 06108
36. CTR Reading Room, c/o A. N. Kaufman, Physics Department, University of California, Berkeley, CA 94720
37. J. N. Davidson, School of Nuclear Engineering, Georgia Institute of Technology, Atlanta, GA 30332
38. S. O. Dean, Director, Fusion Energy Development, Science Applications, Inc., 2 Professional Drive, Suite 249, Gaithersburg, MD 20760
39. Documentation S.I.G.N., Département de la Physique du Plasma et de la Fusion Contrôlée, Association EURATOM-CEA sur la Fusion, Centre d'Études Nucléaires, B.P. 85, Centre du Tri, 38041 Cedex, Grenoble, France
40. W. R. Ellis, Office of Fusion Energy, G-234, Department of Energy, Washington, DC 20545

41. H. K. Forsen, Exxon Nuclear Co., Inc., 777 106th Avenue, N.E.,
C-000777, Bellevue, WA 98009
42. H. P. Furth, Princeton Plasma Physics Laboratory, Princeton
University, Forrestal Campus, P.O. Box 451, Princeton, NJ 08540
43. R. W. Gould, California Institute of Technology, Mail Stop 116-81,
Pasadena, CA 91125
44. R. Grimm, Princeton Plasma Physics Laboratory, Princeton University,
Princeton, NJ 08540
45. B. Grossmann, Courant Institute of Mathematics and Science, New York
University, 251 Mercer Street, New York, NY 10012
46. R. L. Hirsch, Exxon Research and Engineering, P.O. Box 101, Florham
Park, NJ 07932
47. R. A. Huse, Manager, Research and Development, Public Service Gas
and Electric Company, 80 Park Place, Newark, NJ 07101
48. V. E. Ivanov, Physical-Technical Institute of the Ukrainian SSR
Academy of Sciences, 310108 Kharkov, U.S.S.R.
49. A. Kadish, Office of Fusion Energy, G-234, Department of Energy,
Washington, DC 20545
50. B. B. Kadomtsev, I. V. Kurchatov Institute of Atomic Energy, Moscow,
U.S.S.R.
51. E. T. Karlson, Department of Technology, Box 534, S-75121 Uppsala,
Sweden
52. Y. Kiwamoto, Research Institute for Energy Materials, Yokohama
National University, Yokohama 232, Japan
53. R. N. Kostoff, Office of Fusion Energy, Department of Energy, Room
509, 401 First Street NW, Washington, DC 20545
54. L. M. Kovrizhnikh, Lebedev Institute of Physics, Academy of Sciences
of the U.S.S.R., Leninsky Prospect 53, Moscow, U.S.S.R.
55. K. Lackner, Max Planck Institut fur Plasmaphysik, D-8046 Garching
bei München, Federal Republic of Germany
56. G. Laval, Groupe de Physique Théorique, Ecole Polytechnique, 91
Palaiseau, Paris, France
57. Library, Centre de Recherches en Physique des Plasma, 21 Avenue des
Bains, 1007, Lausanne, Switzerland
58. Library, Culham Laboratory, United Kingdom Atomic Energy Authority,
Abingdon, Oxon, OX14 3DB, United Kingdom
59. Library, FOM-Institut voor Plasma-Fysica, Rijnhuizen, Jutphaas,
Netherlands
60. Library, Institute for Plasma Physics, Nagoya University, Nagoya,
Japan 464
61. Library, International Centre for Theoretical Physics, Trieste,
Italy
62. Library, Laboratorio Gas Ionizzati, Frascati, Italy
63. J. G. Lominadze, Academy of Sciences of the Georgian S.S.R.,
8 Dzerzhinski St., 38004, Tbilisi, U.S.S.R.
64. O. P. Manley, Office of Fusion Energy, G-234, Department of Energy,
Washington, DC 20545
65. D. G. McAlees, Exxon Nuclear Co., Inc., 777 106th Avenue, NE,
Bellevue, WA 98009
66. J. E. McCune, School of Engineering, Department of Aeronautics and
Astronautics, Bldg. 37-391, Massachusetts Institute of Technology,
Cambridge, MA 02139

67. A. T. Mense, Subcommittee on Energy Research and Production, B-374, Rayburn House Office Building, Washington, DC 20515
68. C. Mercier, Service du Theorie des Plasmas, Centre d'Études Nucléaires, Fontenay-aux-Roses (Seine), France
69. S. V. Mirnov, I. V. Kurchatov Institute of Atomic Energy, Moscow, U.S.S.R.
70. D. A. Monticello, Princeton Plasma Physics Laboratory, Princeton University, Princeton, NJ 08540
71. K. Nishikawa, Institute for Fusion Theory, Hiroshima University, Higashisendamachi, Hiroshima, Japan
72. B. Outten, Jr., Western Metal Products Company, 1300 Weber Street, Orlando, FL 32803
73. R. E. Papsco, Grumman Aerospace Corp., 101 College Road, Princeton, NJ 08540
74. O. Petrus, Supervisor, C.T.R. Theory Group, Plasma Physics Laboratory, AL. I. CUZA University, Iasi, Romania, 6600
75. R. Pellat, Groupe de Physique Theorique, Ecole Polytechnique, 91 Palaiseau, France
76. D. Pfirsch, Institute for Plasma Physics, 8046 Garching bei München, Federal Republic of Germany
77. Plasma Physics Library, c/o P. Rosenau, Department of Mechanical Engineering, Technion-Israel, Institute of Technology, Haifa, Israel
78. Plasma Physics Group, Department of Engineering Physics, Australian National University, P.O. Box 4, Canberra A.C.T. 2600, Australia
79. O. P. Pogutse, I. V. Kurchatov Institute of Atomic Energy, Moscow, U.S.S.R.
80. A. Popov, Computer Mathematics and Cybernetics Faculty, Moscow State University, Moscow, U.S.S.R.
81. D. C. Robinson, Culham Laboratory, Abingdon, Oxon, OX14, 3DB, United Kingdom
82. A. Rogister, Institute for Plasma Physics, KFA, Postfach 1913, D-5170, Jülich 1, Federal Republic of Germany
83. M. N. Rosenbluth, School of Natural Science, Institute of Advanced Study, Princeton, NJ 08540
84. P. H. Rutherford, Princeton Plasma Physics Laboratory, Princeton University, Princeton, NJ 08540
85. W. Sadowski, Office of Fusion Energy, G-234, Department of Energy, Washington, DC 20545
86. N. R. Sauthoff, Princeton Plasma Physics Laboratory, Princeton University, Princeton, NJ 08540
87. V. D. Shafranov, I. V. Kurchatov Institute of Atomic Energy, 46, Ulitsa Kurchatova, P.O. Box 3402, Moscow, U.S.S.R.
88. Y. S. Sigov, Institute of Applied Mathematics of the U.S.S.R. Academy of Sciences, Miuskaya, Sq. 4, Moscow A-47, U.S.S.R.
89. P. Smeulders, Institute für Plasmaphysik, D-8046 Garching bei München, Republic of Germany
90. W. M. Stacey, Jr., School of Nuclear Engineering, Georgia Institute of Technology, Atlanta, GA 30332
91. T. Stix, Princeton Plasma Physics Laboratory, Princeton University, Princeton, NJ 08540
92. H. R. Strauss, Fusion Research Center, University of Texas at Austin, Austin, TX 78712

93. V. I. Tereshin, Physico-Technical Institute of the Ukrainian SSR Academy of Sciences, Kharkov, 310108 Kharkov, U.S.S.R.
94. J. B. Taylor, Culham Laboratory, United Kingdom Atomic Energy Authority, Abingdon, Oxon, OX14 3DB, United Kingdom
95. Thermonuclear Library, Japan Atomic Energy Research Institute, Tokai, Naka, Ibaraki, Japan
96. K. Toi, Institute of Plasma Physics, Nagoya University, Nagoya, Japan
97. K. Uo, Plasma Physics Laboratory, Kyoto University, Gokasho, Uji, Kyoto, Japan
98. F. Verdaguer, Director, Division of Fusion, Junta de Energia Nuclear, Madrid 3, Spain
99. J. A. Wesson, Culham Laboratory, Abingdon, Oxon, OX14 3DB, United Kingdom
100. Office of Assistant Manager, Energy Research and Development, Department of Energy, Oak Ridge Operations Office, Oak Ridge, TN 37830
- 101-279. Given distribution as shown in TID-4500, Magnetic Fusion Energy (Distribution Category UC-20 g, Theoretical Plasma Physics)